

## Synergistic chemo-photothermal suppression of cancer by melanin decorated MoO<sub>x</sub> nanosheets

Yu Li, Jianrong Wu, Gareth R. Williams, Shiwei Niu, Jianfeng Zhou, Yanbo Yang, Xuejing Zhang, Zi Fu, Dejian Li, and Limin Zhu

*ACS Appl. Bio Mater.*, **Just Accepted Manuscript** • DOI: 10.1021/acsabm.9b00600 • Publication Date (Web): 29 Aug 2019

Downloaded from [pubs.acs.org](https://pubs.acs.org) on August 30, 2019

### Just Accepted

“Just Accepted” manuscripts have been peer-reviewed and accepted for publication. They are posted online prior to technical editing, formatting for publication and author proofing. The American Chemical Society provides “Just Accepted” as a service to the research community to expedite the dissemination of scientific material as soon as possible after acceptance. “Just Accepted” manuscripts appear in full in PDF format accompanied by an HTML abstract. “Just Accepted” manuscripts have been fully peer reviewed, but should not be considered the official version of record. They are citable by the Digital Object Identifier (DOI®). “Just Accepted” is an optional service offered to authors. Therefore, the “Just Accepted” Web site may not include all articles that will be published in the journal. After a manuscript is technically edited and formatted, it will be removed from the “Just Accepted” Web site and published as an ASAP article. Note that technical editing may introduce minor changes to the manuscript text and/or graphics which could affect content, and all legal disclaimers and ethical guidelines that apply to the journal pertain. ACS cannot be held responsible for errors or consequences arising from the use of information contained in these “Just Accepted” manuscripts.

1  
2  
3  
4 **Synergistic chemo-photothermal suppression of cancer by melanin decorated**  
5  
6 **MoO<sub>x</sub> nanosheets**

7  
8  
9 Yu Li<sup>a,1</sup>, Jianrong Wu<sup>a,1</sup>, Gareth R. Williams<sup>b</sup>, Shiwei Niu<sup>a</sup>, Jianfeng Zhou<sup>c</sup>, Yanbo  
10  
11 Yang<sup>a</sup>, Xuejing Zhang<sup>a</sup>, Zi Fu<sup>a</sup>, Dejian Li<sup>d,\*</sup>, Li-Min Zhu<sup>a,\*</sup>  
12  
13  
14

15  
16  
17 <sup>a</sup> College of Chemistry, Chemical Engineering and Biotechnology, Donghua  
18  
19 University, Shanghai, 201620, China  
20  
21

22 <sup>b</sup> UCL School of Pharmacy, University College London, 29-39 Brunswick Square,  
23  
24 London, WC1N 1AX, UK  
25  
26

27 <sup>c</sup> Research Center for Analysis and Measurement, Donghua University, Shanghai  
28  
29 201620, People's Republic of China  
30  
31

32 <sup>d</sup> Department of Orthopedics, Shanghai Pudong Hospital, Fudan University Pudong  
33  
34 Medical Center, Shanghai, 201301, China  
35  
36  
37  
38  
39

40 **\* Corresponding authors.**

41  
42  
43 E-mail: [lzhu@dhu.edu.cn](mailto:lzhu@dhu.edu.cn) (L.-M. Zhu), [lidgejian880820@163.com](mailto:lidgejian880820@163.com) (D. Li).  
44

45  
46 Tel: +862167792655 (L.-M. Zhu);  
47  
48  
49

50  
51 <sup>1</sup> These authors contributed equally.  
52  
53  
54

55  
56 **KEYWORDS:** MoO<sub>x</sub>, melanin, drug delivery system, photothermal,  
57  
58 two-dimensional nanomaterials, synergistic therapy  
59  
60

**ABSTRACT**

Two-dimensional (2D) nanomaterials able to effectively absorb near-infrared (NIR) radiation have shown considerable potential as multifunctional platforms in the treatment of cancer. Here we report a molybdenum dioxide ( $\text{MoO}_x$ )-based system for synergistic chemo- and photothermal therapy of cancer.  $\text{MoO}_x$  nanosheets were generated via a one-step hydrothermal route, grafted with polyethylene glycol (PEG), and decorated with melanin (Mel), with successful functionalization confirmed by IR spectroscopy. The mean diameter and thickness of the  $\text{MoO}_x$  particles are tested found to be  $302 \pm 34$  nm and  $19 \pm 2$  nm using atomic force microscopy. The hydrodynamic size of the  $\text{MoO}_x$  nanosheets was  $105 \pm 17$  nm, and the resulting final  $\text{MoO}_x$ -PEG-Mel-DOX nanocomposites formulation had a uniform diameter of ( $161 \pm 26$  nm). The  $\text{MoO}_x$ -PEG-Mel nanosheets efficiently convert NIR light to heat, possessing a photothermal conversion efficiency of 61.7%. They can also be loaded with doxorubicin (DOX), giving a high drug loading (325.6 mg DOX/g  $\text{MoO}_x$ -PEG-Mel).  $\text{MoO}_x$ -PEG-Mel-DOX shows DOX release influenced by pH and NIR irradiation. Systematic *in vitro* and *in vivo* evaluations reveal that synergistic chemo- and photothermal therapy using  $\text{MoO}_x$ -PEG-Mel-DOX can completely eradicate a tumor, with no observable off-target cytotoxicity. This is the first report of the fabrication of enhanced photothermal agents by combining  $\text{MoO}_x$  nanosheets and a natural product. This work proffers a strategy for efficiently treating cancer, as well as potentially extending the photothermal applications of 2D nanomaterials by surface melanin functionalisation.

## INTRODUCTION

Cancer remains a major healthcare burden worldwide <sup>1</sup>. A variety of treatments, including chemotherapy, surgical resection and laser treatment are available, but typically these come with undesirable side-effects. For instance, chemotherapy is a vital tool for clinicians but has inevitable toxic side effects on healthy tissues and organs, and long-term therapy can lead to the development of resistance to the drug. New treatments are required to ameliorate these issues. Near-infrared (NIR) light-induced photothermal therapy (PTT) has recently emerged as a powerful treatment modality due to its high selectivity and minimal invasiveness <sup>2-9</sup>. PTT requires photothermal agents to convert NIR irradiation into heat and thereby ablate a tumor. Since NIR can be focused locally on the tumor site, this approach can reduce off-target effects. If the delivery system containing the photothermal agent (PTA) is of an appropriate size then the enhanced permeability and retention (EPR) effect allows it to also be selectively accumulated in the tumor area <sup>10-11</sup>. However, the targeting which can be achieved by PTT is imperfect, and effects such as uneven thermal distribution can cause damage to nearby healthy tissue <sup>12-13</sup>. In addition, therapeutic outcomes are constrained by the limited penetration depth of NIR light.

The research boom into of two-dimensional (2D) materials originated accelerated dramatically after from the discovery of graphene in 2004. Over the past decade, a large number of single or multi-layer two-dimensional materials have been studied, they both have unique physical and chemical properties and have showned

1  
2  
3  
4 promising application value explored in many different fields, such as  
5  
6 photoelectronics, energy storage, and transformation and biomedicine. The latter  
7  
8 includes applications in photothermal therapy, and a range of PTAs based on  
9  
10 two-dimensional (2D) nanomaterials have been reported<sup>14-17</sup>. Multifunctional drug  
11  
12 delivery systems based on such 2D systems include those fabricated from graphene  
13  
14 derivatives<sup>18</sup>, MoS<sub>2</sub><sup>15</sup> or WS<sub>2</sub><sup>19</sup>. All these materials exhibit effective absorption in  
15  
16 the NIR region ( $\lambda = 650-1000$  nm), and thus can induce local hyperthermia upon  
17  
18 exposure to NIR light<sup>20</sup>. Loading small molecule drugs onto PTA nanomaterials can  
19  
20 further enhance therapeutic efficiency, as a result of photothermally-mediated drug  
21  
22 release<sup>16, 21-22</sup>.

23  
24  
25  
26  
27  
28  
29  
30 NIR absorption by nonstoichiometric metal chalcogenides is related to the local  
31  
32 surface plasmon resonance<sup>23-25</sup>. Non-stoichiometric molybdenum oxide-based  
33  
34 systems (MoO<sub>x</sub>) are appealing candidate materials for plasmon-based biological  
35  
36 applications owing to their excellent biocompatibility, simple routes to preparation,  
37  
38 and significant NIR absorption<sup>21, 26-27</sup>. In this work, we explored the effects of  
39  
40 coupling MoO<sub>x</sub> with melanin (Mel), a natural biological pigment<sup>28</sup> with strong  
41  
42 absorption in the NIR region<sup>29-31</sup>. We used a simple, cost-effective, single-step route  
43  
44 to prepare MoO<sub>x</sub>, and then modified the resultant nanosheets with poly(ethylene  
45  
46 glycol) (PEG) to enhance stability in the physiological environment<sup>32</sup>. To improve  
47  
48 the photothermal conversion efficacy (PTCE) of the MoO<sub>x</sub>-PEG nanosheets, Mel was  
49  
50 also added to their surfaces. The chemotherapeutic doxorubicin hydrochloride (DOX)  
51  
52 was finally loaded onto the system. The nanoplatform was characterized in detail, and  
53  
54  
55  
56  
57  
58  
59  
60

1  
2  
3  
4 its drug release behavior, *in vitro* toxicity, and *in vivo* efficacy probed. The  
5  
6 experimental strategy underlying the work is illustrated in Scheme 1.  
7  
8  
9

## 10 11 **RESULTS AND DISCUSSION**

12  
13  
14 **Synthesis and characterization of MoO<sub>x</sub> nanocomposites.** Scheme 1 illustrates  
15 the schematic procedure employed for the fabrication of MoO<sub>x</sub>-based drug delivery  
16 systems in this work. First, molybdenum oxide nanosheets were prepared according to  
17 the literature with some modifications<sup>33</sup>. The surface was then modified with PEG  
18 before Mel was added and DOX loaded onto the surface of the nanosheets, resulting  
19 in MoO<sub>x</sub>-PEG-Mel-DOX. The TEM data (Figure 1a) reveal irregularly shaped sheet  
20 structures form after exfoliation. The mean diameter and thickness of the MoO<sub>x</sub>  
21 particles are found to be 302 ± 34 nm and 19 ± 2 nm using AFM (Figure 1b,c). The  
22 hydrodynamic size of the MoO<sub>x</sub> nanosheets was 105 ± 17 nm (Figure 1d). It is  
23 unusual for hydrodynamic sizes to be smaller than those from AFM, but we attribute  
24 this to the dynamic light scattering experiment assuming the particles are spherical,  
25 whereas they actually take the form of platelets. Thus, the hydrodynamic size is  
26 intermediate between the true diameter and thickness of the particles.  
27  
28  
29  
30  
31  
32  
33  
34  
35  
36  
37  
38  
39  
40  
41  
42  
43  
44  
45  
46  
47

48 The valence state of Mo and chemical composition of the MoO<sub>x</sub> nanosheets were  
49 determined by XPS. The XPS survey spectrum of MoO<sub>x</sub> (Figure 2a) indicates the  
50 presence of Mo, O, C, and possibly N (the latter two expected to be from residual  
51 oleylamine). Upon curve fitting and deconvolution, the Mo 3d region reveals four key  
52 peaks: Mo<sup>VI</sup> 3d<sub>3/2</sub>, Mo<sup>V</sup> 3d<sub>3/2</sub>, Mo<sup>VI</sup> 3d<sub>5/2</sub>, and Mo<sup>V</sup> 3d<sub>5/2</sub> (Figure 2b). The sharp peaks  
53  
54  
55  
56  
57  
58  
59  
60

1  
2  
3  
4 at 234.1 and 230.9 eV correspond to the  $3d_{3/2}$  and  $3d_{5/2}$  bands of  $\text{Mo}^{5+}$  respectively.  
5  
6 The broader peaks at 235.7 and 232.5 eV can be attributed to  $\text{Mo}^{6+}$   $3d_{3/2}$  and  $3d_{5/2}$   
7  
8 <sup>34-36</sup>. From calculating the area ratios of  $\text{Mo}^{5+}$  and  $\text{Mo}^{6+}$  the contents of  $\text{Mo}^{5+}$  and  $\text{Mo}^{6+}$   
9  
10 in  $\text{MoO}_x$  are estimated at 49.6% and 50.4%, giving a mean oxidation state of +5.5 and  
11  
12 an empirical formula of  $\text{MoO}_{2.75}$ .  
13  
14  
15

16  
17 The small angle XRD data (Figure S1, Supporting Information) agree with those  
18  
19 previously reported for  $\text{MoO}_x$  <sup>33</sup>. However, neither this nor the wide angle pattern  
20  
21 (Figure S2) match with any of the crystal structures for binary Mo/O compounds  
22  
23 reported in the ICSD. The presence of regularly spaced reflections (at 2.5, 5.0, 7.5°)  
24  
25 indicate the presence of a layered structure with basal reflections at *ca.* 35.3, 17.7, and  
26  
27 11.8 Å. This suggests that the material fabricated comprises an O-deficient  $\text{MoO}_3$   
28  
29 structure (the latter is known to be layered). The very large interlayer spacing can be  
30  
31 ascribed to the incorporation of oleylamine between the  $\text{MoO}_x$  layers. The end-to-end  
32  
33 distance of oleylamine is around 22 Å, and therefore a d-spacing of ~ 35 Å is  
34  
35 consistent with the presence of an intertwined bilayer of oleylamine molecules  
36  
37 between the  $\text{MoO}_x$  layers, with the  $\text{NH}_2$  groups interacting through H-bonding with  
38  
39 the O atoms in the layers.  
40  
41  
42  
43  
44  
45  
46  
47

48 The functionalization of  $\text{MoO}_x$  with PEG and Mel and subsequent loading of DOX  
49  
50 were evaluated by IR and UV-vis spectroscopy, and through zeta potential  
51  
52 measurements. IR spectra are presented in Figure 3a. In the spectrum of  $\text{MoO}_x$ , the  
53  
54 peaks at 640 and 880  $\text{cm}^{-1}$  were correspond to Mo-O-Mo vibrations, and there is  
55  
56 additionally a band at 950  $\text{cm}^{-1}$  from Mo=O <sup>37-41</sup>.  $\text{CH}_2$  vibrations can be seen at  
57  
58  
59  
60

1  
2  
3  
4 around 2950  $\text{cm}^{-1}$  and 1450  $\text{cm}^{-1}$  from the oleylamine in the system. The IR spectrum  
5  
6 of PEG shows particularly distinct bands at 1060 and 1100  $\text{cm}^{-1}$  from -C-O-C-  
7  
8 vibrations. Both can be seen in the  $\text{MoO}_x$ -PEG spectrum, indicating successful  
9  
10 modification. Melanin has C=O functional groups, which result in bands at 1705 and  
11  
12 1607  $\text{cm}^{-1}$ . These characteristic peaks are also observed with both  $\text{MoO}_x$ -PEG-Mel  
13  
14 and  $\text{MoO}_x$ -PEG-Mel-DOX, suggesting successful functionalization with Mel.  
15  
16  
17

18  
19 As would be intuitively expected, the particle size (Figure 1d) becomes  
20  
21 increasingly large at each functionalization step, with the final  $\text{MoO}_x$ -PEG-Mel-DOX  
22  
23 nanosheets being  $163 \pm 27$  nm in size. Zeta potential measurements (Figure 3b) found  
24  
25 that the potential of  $\text{MoO}_x$  is -6.3 mV, but this declines to -26.1 mV after the addition  
26  
27 of PEG because of the existence of ester group in mPEG-DSPE. The potential further  
28  
29 decreases to -43.1 mV after Mel functionalization, as a result of the presence of  
30  
31 ionizable COOH groups in Mel. After DOX is loading, the zeta potential turned to  
32  
33 +17.2 mV because of the amine groups in DOX. The serial changes in zeta potential  
34  
35 following each step in the nanocomposite construction process indicate the successful  
36  
37 formation of  $\text{MoO}_x$ -PEG-Mel-DOX.  
38  
39  
40  
41  
42  
43

44  
45 UV-Vis-NIR spectra (Figure 3c) reveal that the  $\text{MoO}_x$  systems absorb strongly in  
46  
47 the NIR region as expected. The characteristic absorption peaks of DOX at 480 nm  
48  
49 and at 200-250 nm are present in the UV-Vis spectrum of  $\text{MoO}_x$ -PEG-Mel-DOX,  
50  
51 demonstrating successful drug loading. A range of  $\text{MoO}_x$ -PEG-Mel: DOX ratios were  
52  
53 explored, and the DOX loading onto the nanosheets determined from UV-Vis-NIR  
54  
55 spectroscopy (Figure S5). As the ratio of DOX:  $\text{MoO}_x$ -PEG-Mel increased from 1:4 to  
56  
57  
58  
59  
60

1  
2  
3  
4 1:1, the DOX loading capacity increased, reaching a saturation level of 32.5% at a  
5  
6 ratio of 1:1. This formulation was used for all other studies. The loading capacity  
7  
8 noted here is rather greater than a previous literature by Zhang et al. (who prepared a  
9  
10 loading of 151.4 mg per gram of a MoS<sub>2</sub>-PEG nanocomposite) and close to that  
11  
12 reported for graphdiyne (38%)<sup>42-43</sup>. The loading observed here is significantly  
13  
14 improved over other a range of other delivery systems which have been explored in  
15  
16 the literature, such as molecularly imprinted polymers (7.08%), polyprodrug  
17  
18 nanoparticles (13%), or mesoporous silica nanoparticles (5.8%)<sup>44-46</sup>.

19  
20  
21  
22  
23  
24  
25 ***In vitro* drug release.** DOX release was studied at two different pH, with or  
26  
27 without laser irradiation (Figure 3d). The cumulative drug release reached 21.9% and  
28  
29 62.4% at pH 7.4 and pH 5.0, indicating that drug release from MoO<sub>x</sub>-PEG-Mel-DOX  
30  
31 is pH responsive. This can be ascribed to the amino group of DOX being ionized in  
32  
33 acidic conditions, increasing its solubility and encouraging drug release<sup>47</sup>. With the  
34  
35 application of NIR irradiation, DOX release reaches 74.2% in the acidic environment,  
36  
37 again higher than the 34.6% seen in neutral conditions. This increase in release upon  
38  
39 NIR exposure arises because of hyperthermia being induced by laser irradiation. This  
40  
41 increases the vibrational energy of both the MoO<sub>x</sub> nanosheets and DOX, thereby  
42  
43 reducing the strength of interactions between the two and accelerating drug release.  
44  
45 Because the tumor microenvironment has a lower pH than that of normal tissue, such  
46  
47 a drug delivery system is likely to be effective in targeted cancer chemotherapy<sup>42, 48</sup>.

48  
49  
50  
51  
52  
53  
54  
55  
56 **Photothermal effects.** PTT data are presented in Figure 4. The temperature  
57  
58 changes of MoO<sub>x</sub>-PEG and MoO<sub>x</sub>-PEG-Mel suspensions as a function of time were  
59  
60

1  
2  
3  
4 recorded (Figure 4a) and the PTCE of MoO<sub>x</sub>-PEG and MoO<sub>x</sub>-PEG-Mel evaluated  
5  
6 under identical conditions (concentration: 1 mg/mL; power: 1 W/cm<sup>2</sup> for 5 min). The  
7  
8 PTCE ( $\eta$ ) of MoO<sub>x</sub>-PEG and MoO<sub>x</sub>-PEG-Mel are respectively 44% (Figure S3) and  
9  
10 61.7% (Figure 4b). These values are notably higher than reported data for other PTAs  
11  
12 (e.g. graphene oxide at 25%, antimony quantum dots at 45.5%, or a black phosphorus  
13  
14 analogue compound at 39.3%)<sup>49-51</sup>.

15  
16  
17  
18  
19 The temperature changes for aqueous suspensions of MoO<sub>x</sub>-PEG-Mel-DOX at  
20  
21 different concentrations were next measured (Figure 4c). Compared with pure water,  
22  
23 the MoO<sub>x</sub>-PEG-Mel-DOX dispersions display increasing temperatures as the  
24  
25 concentration is increased. Temperatures can reach 67.9 °C after laser irradiation for 5  
26  
27 min (1 mg/mL; power: 1 W/cm<sup>2</sup>). Laser power density-dependent temperature  
28  
29 increases are also seen with MoO<sub>x</sub>-PEG-Mel-DOX suspensions (Figure 4d). The  
30  
31 enhancement in the photothermal efficiency after decoration of MoO<sub>x</sub> with Mel is  
32  
33 clear from the thermal imaging data (Figure 4e). In previous studies with similar  
34  
35 systems rather lower PTCEs have been observed, with 22.6% reported for MoO<sub>3-x</sub>  
36  
37 hollow nanospheres and 27.3% for MoO<sub>x</sub> nanoparticles<sup>21, 27</sup>. The  
38  
39 MoO<sub>x</sub>-PEG-Mel-DOX system can reach a higher temperature in a reduced time  
40  
41 period, and thus can potentially kill tumor cells more quickly while reducing damage  
42  
43 to normal tissues<sup>52-53</sup>.

44  
45  
46  
47  
48 For therapeutic applications, the stability of the system over repeated cycles of NIR  
49  
50 irradiation is crucial. We find that MoO<sub>x</sub>-PEG-Mel-DOX maintains its potent PTT  
51  
52 properties, and a strong and unchanged temperature response is observed over five  
53  
54  
55  
56  
57  
58  
59  
60

1  
2  
3  
4 cycles of illumination (Figure S4). Overall, these findings indicate that the  
5  
6 MoO<sub>x</sub>-PEG-Mel-DOX nanomaterial has good prospects for use in photothermal  
7  
8 therapy.  
9

10  
11 **Cellular uptake and intracellular DOX release.** CLSM data are presented in  
12  
13 Figure 5a. The presence of both DOX (red) and DAPI (blue) fluorescence, the images  
14  
15 show that MoO<sub>x</sub>-PEG-Mel-DOX could be extensively taken up by cancer cells. In  
16  
17 contrast, the free DOX showed relatively weak intracellular red fluorescence  
18  
19 compared with the MoO<sub>x</sub>-PEG-DOX groups, with or without NIR laser irradiation.  
20  
21 This can be ascribed to increased uptake of MoO<sub>x</sub>-PEG-Mel nanosheets. For the  
22  
23 NIR-treated MoO<sub>x</sub>-PEG-Mel-DOX group, the intracellular red fluorescence was  
24  
25 significantly enhanced, which is expected to result from the hyperthermia generated  
26  
27 by the NIR laser. This causes the cell membrane to become slightly damaged, and the  
28  
29 nanomaterial uptake to increase. Hyperthermia also promotes the release of DOX  
30  
31 from the drug delivery system. Further investigation of MoO<sub>x</sub>-PEG-Mel-DOX  
32  
33 internalization by 4T1 cells was performed with the aid of flow cytometry. Figure S6  
34  
35 shows that the intracellular DOX fluorescence intensity of cells treated with  
36  
37 MoO<sub>x</sub>-PEG-Mel-DOX after laser irradiation was significantly stronger than for those  
38  
39 cells not receiving a laser treatment, confirming that NIR-facilitated the intracellular  
40  
41 release of DOX and uptake of MoO<sub>x</sub>-PEG-Mel-DOX nanosheets.  
42  
43  
44  
45  
46  
47  
48  
49  
50  
51

52  
53 ***In vitro* cell viability.** The cytotoxicity of MoO<sub>x</sub>-PEG and MoO<sub>x</sub>-PEG-Mel with  
54  
55 4T1 cells was conducted by using the MTT assay. As can be seen from Figure 5b, cell  
56  
57 survival rates are high, and even at 200 µg/mL the viability is > 80%. The carrier  
58  
59  
60

1  
2  
3  
4 materials hence appear to be very biocompatible. We next explored the potential of  
5  
6 the systems in *in vitro* photothermal and chemotherapeutic cell killing experiments.  
7  
8  
9 The results can be found in Figure 5c. In all cases, dose-dependent cytotoxic effects  
10  
11 are seen. Free DOX is the least effective of the treatments, with cell viability still at  
12  
13 *ca.* 40% when a concentration of 10  $\mu\text{g/mL}$  was used.  $\text{MoO}_x\text{-PEG-Mel-DOX}$  without  
14  
15 laser irradiation causes somewhat more cell death than free DOX. The application of  
16  
17 NIR irradiation causes somewhat more cell death than free DOX. The application of  
18  
19 NIR irradiation markedly increases cell death, with both  $\text{MoO}_x\text{-PEG-Mel}$  and  
20  
21  $\text{MoO}_x\text{-PEG}$  and NIR administration leading to greater cell death than the  
22  
23 DOX-containing systems without NIR exposure. Still greater cell death is observed  
24  
25 when the  $\text{MoO}_x\text{-PEG-Mel-DOX}$  system is combined with NIR: this treatment gave  
26  
27 the lowest cell viability values. When the concentration of DOX was 10  $\mu\text{g/mL}$ , the  
28  
29 viability of cells given free DOX and  $\text{MoO}_x\text{-PEG-Mel-DOX}$  were 39% and 30.7%.  
30  
31 Those treated with  $\text{MoO}_x\text{-PEG+NIR}$  had a survival rate of 24.9%, while the  
32  
33  $\text{MoO}_x\text{-PEG-Mel}$  group viability was 8.1% and the synergistic treatment led to only  
34  
35 2.3% cell survival. The half maximal inhibitory concentration ( $\text{IC}_{50}$ ) of  
36  
37  $\text{MoO}_x\text{-PEG-Mel-DOX}$  is 2.31  $\mu\text{g/mL}$ , much less than the free DOX (6.27  $\mu\text{g/mL}$ ).  
38  
39 This is presumably a result of the greater extent of uptake of the  
40  
41  $\text{MoO}_x\text{-PEG-Mel-DOX}$  nanosheets. For the combined treatment comprising  
42  
43  $\text{MoO}_x\text{-PEG-Mel-DOX}$  with NIR irradiation, the  $\text{IC}_{50}$  is 0.028  $\mu\text{g/mL}$ , as a result of  
44  
45 the synergistic chemo-photothermal therapy.  
46  
47  
48  
49  
50  
51  
52  
53  
54

55  
56 To further evaluate the ability of the nanocomposites to kill cancer cells, 4T1 cells  
57  
58 were stained with CA and PI. This permits us to distinguish between live (green) and  
59  
60

1  
2  
3  
4 apoptotic (red) cells (Figure 5d). Cells treated with PBS showed only very small  
5  
6 amounts of cell death, while increased apoptosis was noted with cells exposed to other  
7  
8 treatments. The greatest extent of cell death was observed with  
9  
10 MoO<sub>x</sub>-PEG-Mel-DOX and NIR laser irradiation. The NIR both causes temperature  
11  
12 increases through photothermal conversion, and also weakens the interactions  
13  
14 between DOX and the MoO<sub>x</sub> carrier <sup>42</sup>. This synergistic effect leads to the greatest  
15  
16 extent of cell death when both PTT and chemotherapy are applied.  
17  
18  
19  
20  
21

22 Compared with previously published studies using MoS<sub>2</sub> as the PTA <sup>16, 42</sup>, the  
23  
24 MoO<sub>x</sub> composites here are more potent in inducing cell death. With NIR irradiation  
25  
26 and an equivalent DOX concentration of 10 μg mL<sup>-1</sup>, MoS<sub>2</sub> materials leave more than  
27  
28 10% of cells alive, while here the survival rate was only 2.3% with an analogous  
29  
30 treatment. This can be attributed to the higher PTCE of the MoO<sub>x</sub> nanoplatform and  
31  
32 its greater drug loading capacity.  
33  
34  
35  
36  
37

38 ***In vivo* antitumor efficacy.** 4T1 tumor-bearing mice were randomly assigned to  
39  
40 one of five groups: ( I ) control (saline); ( II ) free DOX; ( III ) MoO<sub>x</sub>-PEG-Mel-DOX;  
41  
42 (IV) MoO<sub>x</sub>-PEG-Mel+NIR; and, ( V ) MoO<sub>x</sub>-PEG-Mel-DOX+NIR. During the  
43  
44 treatment period, there was no significant weight loss in animals treated with the  
45  
46 MoO<sub>x</sub> nanocomposites, indicating a lack of toxicity (Figure 6a). In contrast, a steady  
47  
48 loss in weight was seen in the free DOX group. This effect arises owing to the  
49  
50 off-target effects of the drug. The sizes of the tumors grow continuously throughout  
51  
52 the experiment when the mice were given DOX or saline (Figure 6b), and small  
53  
54 increases are seen with MoO<sub>x</sub>-PEG-Mel-DOX and MoO<sub>x</sub>-PEG-Mel+NIR treatment.  
55  
56  
57  
58  
59  
60

1  
2  
3  
4 A decline in the tumor volume to virtually zero is noted in the  
5  
6 MoO<sub>x</sub>-PEG-Mel-DOX+NIR group. The animals were euthanized after 21 days and  
7  
8 the tumors excised and photographed (Figure 6c). These images verify the results in  
9  
10 Figure 6b, with the smallest tumors being from mice receiving  
11  
12 MoO<sub>x</sub>-PEG-Mel-DOX+NIR. Kaplan-Meier survival curves (Figure 6d) show that the  
13  
14 survival time of the mice given synergistic PTT-chemotherapy was markedly longer  
15  
16 than the other groups.  
17  
18  
19  
20  
21

22 **Histological analysis.** After the processing of treatment, the major organs and  
23  
24 tumors of the mice were excised and H&E staining used to investigate the *in vivo*  
25  
26 toxicity and therapeutic effects of the different groups. Compared to the control  
27  
28 group, large areas of necrotic and apoptotic cells in the tumor area (brown dots) can  
29  
30 be observed in the synergistic treatment group by TUNEL staining (Figure 6e). The  
31  
32 same conclusions can be drawn from the hematoxylin and eosin (H&E) staining  
33  
34 (Figure 6e).  
35  
36  
37  
38  
39

40 There was no significant inflammation, apoptosis or necrosis observed in sections  
41  
42 of the major organs ( spleen, liver, heart, lung and kidney) in the case of the groups  
43  
44 treated with the nanosheets. In the images from the free DOX group the the  
45  
46 glomerular cells of the kidney show visible congestion, and also slight focal  
47  
48 inflammation in the liver (indicating hepatocellular vesicular steatosis) (Figure 7) <sup>48</sup>,  
49  
50  
51 <sup>54</sup>. These findings reveal that the MoO<sub>x</sub>-PEG-Mel-DOX nanoplatform has low  
52  
53 off-target toxicity and good biocompatibility, which renders it appropriate for  
54  
55 prolonged treatment regimens such as those required to treat cancer.  
56  
57  
58  
59  
60

1  
2  
3  
4       ***In vivo* Biodistribution.** A biodistribution study was performed by measuring the  
5  
6 Mo concentrations in different organs of mice at selected time points after intravenous  
7  
8 injection of MoO<sub>x</sub>-PEG-Mel-DOX (Figure S7). After one day, Mo is mainly  
9  
10 concentrated in the liver, spleen and lungs, because of recognition of the nanosheets  
11  
12 by the reticuloendothelial system. The presence of Mo in the major organs rapidly  
13  
14 decreases with time, and reaches a very low level on the seventh day. This suggests  
15  
16 that the MoO<sub>x</sub> nanosheets can be quickly excreted after administration, and do not  
17  
18 accumulate *in vivo*.  
19  
20  
21  
22  
23

24       **Discussion.** The new PTT system developed in this work has a number of  
25  
26 advantages over others previously reported in the literature. First, compared with the  
27  
28 cumbersome multi-step process required to generate MoS<sub>2</sub> and Ti<sub>3</sub>C<sub>2</sub> and the low  
29  
30 yield typically seen with antimony quantum dots, the MoO<sub>x</sub> system is prepared by a  
31  
32 facile hydrothermal approach and can be produced in bulk. Compared with other  
33  
34 MoO<sub>x</sub> materials that have been reported<sup>21, 27</sup>, the MoO<sub>x</sub>-PEG-Mel-DOX system has a  
35  
36 higher PTCE, so the temperature can be raised more rapidly to kill tumor cells and  
37  
38 reduce damage to normal tissues. DOX release is responsive both to pH and NIR  
39  
40 irradiation, meaning that the systems have the potential to be used to specifically  
41  
42 target tumor tissue. The literature is clear that MoO<sub>x</sub> materials have good *in vivo*  
43  
44 biocompatibility and better biodegradability than MoS<sub>2</sub><sup>26-27, 33, 55</sup>, which concurs with  
45  
46 the findings from this study. Overall therefore, it appears that the MoO<sub>x</sub> systems have  
47  
48 great potential for targeted cancer therapeutics.  
49  
50  
51  
52  
53  
54  
55  
56  
57  
58  
59  
60

## CONCLUSIONS

Here we report melanin decorated MoO<sub>x</sub> nanosheets prepared via a one-pot hydrothermal method. These were loaded with doxorubicin (DOX) and explored for combined photothermal (PTT)-chemotherapy. The combination of melanin and MoO<sub>x</sub> endows the nanoplatform with a high photothermal conversion efficiency (61.7%). The drug-loaded MoO<sub>x</sub>-PEG-Mel-DOX nanoparticles possess a uniform size (163 ± 13 nm) and high drug loading capacity (325.6 mg/g MoO<sub>x</sub>-PEG-Mel). Drug release from MoO<sub>x</sub>-PEG-Mel-DOX was responsive to both pH and NIR laser irradiation. *In vitro* experiments demonstrate that the MoO<sub>x</sub>-PEG-Mel-DOX nanoplatform effectively kills breast cancer cells *via* synergistic chemo- and PTT. In addition, *in vivo* therapeutic evaluations in a murine xenograft breast cancer model revealed a complete suppression of tumor growth when mice were given synergistic chemo/PTT therapy. Systematic *in vivo* biocompatibility assays showed MoO<sub>x</sub>-PEG-Mel-DOX to have very good biocompatibility, with no off-target toxicity observed. Overall, the findings indicate that the MoO<sub>x</sub>-PEG-Mel-DOX nanoplatform has bright prospect in cancer therapy.

## EXPERIMENTAL SECTION

**Materials and reagents:** Ammonium molybdate tetrahydrate [(NH<sub>4</sub>)<sub>6</sub>Mo<sub>7</sub>O<sub>24</sub>·4H<sub>2</sub>O], oleylamine (80-90%), and doxorubicin hydrochloride (DOX) were obtained from Aladdin Co., Ltd. Melanin, 3-(4,5-dimethyl-thiazol-yl)-2,5-diphenyltetrazolium bromide (MTT), phosphate

1  
2  
3  
4 buffered saline (PBS) and calcein AM (CA), propidium iodide (PI) were supplied by  
5  
6 Sigma Aldrich. Polyethylene glycol (mPEG-DSPE, Mw = 2000) was purchased from  
7  
8 Shanghai YaYi Co., Ltd. Cyclohexane and aqueous hydrochloric acid (37.5 wt %) were  
9  
10 acquired from the Sinopharm Chemical Reagent Co., Ltd. 4T1 cells were  
11  
12 obtained from the Type Culture Collection of the Chinese Academy of Sciences. Fetal  
13  
14 bovine serum (FBS), Dulbecco's Modified Eagle Medium (DMEM), trypsin-EDTA,  
15  
16 penicillin and streptomycin were acquired from Gibco. A hematoxylin and eosin  
17  
18 staining kit was sourced from Shanghai Weiao Biotechnology Co, and a terminal  
19  
20 deoxynucleotidyl transferase dUTP nick end labeling (TUNEL) apoptosis detection  
21  
22 kit from Beyontime. Distilled water was employed throughout.  
23  
24  
25  
26  
27  
28  
29

30 **Synthesis of MoO<sub>x</sub> nanosheets.** These were prepared through a simple  
31  
32 hydrothermal process. Ammonium molybdate (3 g) was dispersed in distilled water  
33  
34 (30 mL), while hydrochloric acid (1.5 mL, 1 mol/L) and oleylamine (2 g) were  
35  
36 dissolved in cyclohexane (10 mL). The two liquids were then mixed slowly under  
37  
38 stirring for 30 min, resulting in the formation of a white solid. The dispersion was  
39  
40 placed in an autoclave (50 mL) and conducted at 180°C for 14 h. A blue precipitate  
41  
42 was obtained after this hydrothermal process. The precipitate was washed with  
43  
44 chloroform and ethanol and recovered by centrifugation.  
45  
46  
47  
48  
49

50 **Preparation of MoO<sub>x</sub>-PEG nanosheets.** For PEGylation, 10 mg of MoO<sub>x</sub> was  
51  
52 finely ground in a pestle and mortar and then mixed with 40 mL of chloroform. This  
53  
54 dispersion was cooled in an ice bath and a probe sonicator (SL-400sS, Nanjing  
55  
56 Shunliu Instruments) used to exfoliate the solid. Next, 50 mg of mPEG-DSPE was  
57  
58  
59  
60

1  
2  
3  
4 dispersed into the MoO<sub>x</sub> suspension. The mixture obtained was stirred at room  
5  
6 temperature for 12 h. The chloroform was removed by rotary evaporation, and the  
7  
8 residual solid dispersed in deionized water under sonication. MoO<sub>x</sub>-PEG was isolated  
9  
10 by centrifugation before being washed with distilled water (30 mL).  
11  
12

13  
14 **Preparation of MoO<sub>x</sub>-PEG-Mel nanosheets.** MoO<sub>x</sub>-PEG nanosheets (20 mg)  
15  
16 were dispersed into distilled water (30 mL) and Mel (4 mg) was added under  
17  
18 ultrasonication, followed by stirring for 12 h. The MoO<sub>x</sub>-PEG-Mel nanosheets were  
19  
20 isolated by centrifugation and then washed with distilled water (30 mL) three times.  
21  
22

23  
24 **Drug loading.** DOX (20 mg) was dissolved in distilled water (40 mL) and  
25  
26 MoO<sub>x</sub>-PEG-Mel (20 mg) added, with ultrasonication performed for 5 min to form a  
27  
28 homogeneous suspension. This was followed by stirring for 12 h in the dark. The  
29  
30 solid was splitted by centrifugation and purified by washing with distilled water (30  
31  
32 mL). The supernatants were collected and used to quantify the loading capacity of the  
33  
34 system via UV-Vis spectroscopy at 480 nm.  
35  
36  
37  
38

39  
40 **Materials characterization.** The particle habit of MoO<sub>x</sub> was studied on a  
41  
42 transmission electron microscope (TEM; JEM-2100, JEOL). The dimensions of the  
43  
44 MoO<sub>x</sub>-PEG nanosheets were quantified using a 5500 atomic force microscope (AFM;  
45  
46 Agilent). A BI-200SM instrument (Brookhaven) was employed to collect dynamic  
47  
48 light scattering (DLS) data, and a ZS90 Zetasizer (Malvern Instruments) for zeta  
49  
50 potential measurements. UV-Vis spectrum was collected on a Shanghai JingHua  
51  
52 Instruments UV-1800 spectrophotometer. IR spectra were obtained with the aid of a  
53  
54 Nexus 870 spectrometer (Nicolet Instruments Inc). X-ray diffraction (XRD) patterns  
55  
56  
57  
58  
59  
60

1  
2  
3  
4 were obtained on a Bruker D8 Advance diffractometer. This is supplied with Cu K $\alpha$   
5  
6 radiation ( $\lambda=1.5418 \text{ \AA}$ ). The chemical composition of MoO $_x$  was explored by X-ray  
7  
8 photoelectron spectroscopy (XPS), and spectra produced using an Escalab 250Xi  
9  
10 instrument. The PTCE of the MoO $_x$ -PEG and MoO $_x$ -PEG-Mel nanosheets were  
11  
12 quantified with an 808 nm laser apparatus (Shanghai Xilong Optoelectronics  
13  
14 Technology Co) and the temperature variation of the dispersion was recorded using a  
15  
16 thermocouple connected to a digital thermometer (DT-8891E, Shenzhen Everbest  
17  
18 Machinery Industry).  
19  
20  
21  
22  
23

24 **Photothermal effects.** To explore the photothermal effects of  
25  
26 MoO $_x$ -PEG-Mel-DOX, various concentrations of the samples were irradiated (808  
27  
28 nm, 1.0 W cm $^{-2}$ ) for 5 min. The effect of laser power density was investigated by  
29  
30 exposing a suspension of MoO $_x$ -PEG-Mel-DOX (1.0 mg mL $^{-1}$ ) to different densities  
31  
32 from 0.25 to 1.50 W cm $^{-2}$ . Water was employed as a control and exposed to the same  
33  
34 conditions. The NIR laser stability of MoO $_x$ -PEG-Mel-DOX was evaluated under  
35  
36 irradiation for 5 min (1.0 W cm $^{-2}$ ) with five laser on-off cycles. In all cases,  
37  
38 temperature changes of the suspension were recorded through an infrared thermal  
39  
40 imaging system (FLIR A300, Shanghai Spectrum Electronics Technology Co). The  
41  
42 volume of dispersion used for each experiment was 200  $\mu$ L, and therefore the  
43  
44 temperature of the suspension can be assumed to be constant throughout. The PTCE  
45  
46 was figured by using the equation:  
47  
48  
49  
50  
51  
52  
53

$$\eta = \frac{hS(T_{\max} - T_{\text{am}}) - Q^0}{I(1 - 10^{-A})}$$

54  
55  
56  
57  
58  
59  
60  
S and h represent the surface area and the heat transfer coefficient. T $_{\max}$  is the

1  
2  
3  
4 equilibrium temperature and  $T_{\text{am}}$  the ambient temperature,  $Q_0$  the heat absorption of  
5  
6 the quartz container,  $I$  the laser power density (250 mW), and  $A$  the absorbancy of the  
7  
8 samples at 808 nm <sup>56</sup>.

9  
10  
11 ***In vitro* drug release.** 3 mL of a suspension of MoO<sub>x</sub>-PEG-Mel-DOX (1.0 mg/mL)  
12  
13 in PBS (pH 7.4 or 5.0) was placed in a dialysis bag (MWCO=8-10 kDa) and dialyzed  
14  
15 against PBS at the same pH (40 mL) under stirring. Periodically, 1 mL aliquots were  
16  
17 collected and an equal volume of fresh-preheated PBS was added. The concentration  
18  
19 of DOX in the release aliquots was quantified at 480 nm by UV-Vis spectroscopy.  
20  
21 Where laser treatment was undertaken, the formulations were irradiated for 5 min  
22  
23 (808 nm, 1 W/cm<sup>2</sup>) at selected timepoints (1, 5, 12, 24, 48, and 60 h).  
24  
25  
26  
27  
28  
29

30 **Cellular uptake and intracellular DOX release.** The cellular uptake of  
31  
32 MoO<sub>x</sub>-PEG-Mel-DOX was studied using confocal laser scanning microscopy  
33  
34 (CLSM). The 4T1 cell was incubated in a 24-well plate (1×10<sup>5</sup> cells each well in 1  
35  
36 mL of medium) and cultured for 24 h at 37°C and 5% CO<sub>2</sub>. The media was aspirated  
37  
38 and a suspension of PBS, free DOX, MoO<sub>x</sub>-PEG-Mel-DOX (150 μL, final DOX  
39  
40 concentration = 5 μg mL<sup>-1</sup>) was added, with or without the application of NIR  
41  
42 irradiation, and the cells were further incubated in DMEM for 3 h. Next, the 4T1 cells  
43  
44 were washed for three times with PBS (pH 7.4, 10 min each rinse). The DAPI  
45  
46 solution was used to stain cell nuclei and fluorescent images were obtained on an  
47  
48 Eclipse Ti-S microscope (Nikon Ltd, Japan). After trypsinization, these cells were  
49  
50 baptised for three times with PBS and stained with PI to exclude dead cells. Finally,  
51  
52 the intracellular fluorescence of DOX was quantified by flow cytometry (Becton  
53  
54  
55  
56  
57  
58  
59  
60

Dickinson, CA, USA).

***In vitro* cell viability.** 4T1 cells were seeded in DMEM medium supplemented with 1% v/v penicillin, 1% v/v streptomycin, and 10% v/v FBS (“complete DMEM”). The relative cell viabilities were evaluated using the MTT assay. 4T1 cells were cultured in a 96-well plate ( $1 \times 10^4$  cells per well, 150  $\mu$ L of medium) and the cells incubated for 24 h at 37 °C and 5% CO<sub>2</sub>. The medium was then aspirated and the cells washed with PBS. Next, 150  $\mu$ L of suspensions of MoO<sub>x</sub>-PEG-Mel and MoO<sub>x</sub>-PEG in complete DMEM were added to give final concentrations of 0, 1, 5, 10, 50, 100 and 200  $\mu$ g/mL, and the cells were hatched for another 24 h. The medium was removed, MTT solution (20  $\mu$ L; 5 mg mL<sup>-1</sup>) added, and the plate hatched for 4 h. The supernatant was aspirated, and dimethylsulfoxide (DMSO, 150  $\mu$ L) added to each well to dissolve any formazan crystals which had formed. After 20 min, the absorbance at 570 nm was quantified using a microplate reader (MULTISKAN MK3, ThermoFisher). Three independent experiments were performed with five replicates in each.

**Synergistic effects *in vitro*.** 4T1 cells in complete DMEM were seeded in 96-well plates at  $1 \times 10^4$  cells perwell (150  $\mu$ L/well) and incubated for 24 h at 5 % CO<sub>2</sub> / 37 °C. The cells were then exposed to four different treatments: PBS+NIR, MoO<sub>x</sub>-PEG+NIR, MoO<sub>x</sub>-PEG-Mel+NIR, free DOX and MoO<sub>x</sub>-PEG-Mel-DOX with or without laser irradiation. The MTT assay was used to quantify relative cell viabilities. The concentrations of free DOX were set as 0.01, 0.1, 1, 5,10  $\mu$ g/mL, and the MoO<sub>x</sub> systems were added in amounts to give equivalent DOX concentrations. In

1  
2  
3  
4 the case of treatments without DOX, the same mass of nanosheets as with  
5  
6 MoO<sub>x</sub>-PEG-Mel-DOX was used. Suspensions or solutions of the drug were added to  
7  
8 the pre-incubated cells after aspiration. After a further incubation for 24 h, the  
9  
10 treatment medium was aspirated, before the cells were washed with PBS. Fresh  
11  
12 DMEM (150 μL) was then added. In the case of the NIR treatments, the cells were  
13  
14 exposing under an 808 nm NIR laser (1.0 W/cm<sup>2</sup>) for 5 min at this point. In all cases,  
15  
16 after washing the cells were incubated in complete DMEM for next 24 h. Cell  
17  
18 viability was then determined through the MTT assay (three independent experiments,  
19  
20 five replicates in each).  
21  
22  
23  
24  
25

26  
27 **Confocal microscopy.** Confocal experiments were performed with 4T1 cells  
28  
29 exposed to the following treatments: PBS+NIR, MoO<sub>x</sub>-PEG+NIR,  
30  
31 MoO<sub>x</sub>-PEG-Mel+NIR, free DOX, and MoO<sub>x</sub>-PEG-Mel-DOX with or without laser  
32  
33 irradiation. 4T1 cells were seeded in a 24-well plate for 24 h at 37 °C / 5% CO<sub>2</sub> (1 ×  
34  
35 10<sup>4</sup> cells/well, 150 μL of medium). The culture medium was removed and fresh  
36  
37 medium containing MoO<sub>x</sub>-PEG, MoO<sub>x</sub>-PEG-Mel, free DOX (0.1 μg mL<sup>-1</sup>) and  
38  
39 MoO<sub>x</sub>-PEG-Mel-DOX (with equivalent DOX concentrations of 0.1 μg mL<sup>-1</sup>) added,  
40  
41 before the cells were incubated for another 24 h. The 4T1 cells were next scoured  
42  
43 with PBS and complete DMEM medium (150 μL) was then put into it. Where  
44  
45 required, the cells were exposed to a laser (808 nm, 1 W cm<sup>-2</sup>) for 5 min at this point.  
46  
47 After 2 h incubation, the 4T1 cells were stained with CA and PI for another 15 min  
48  
49 and imaged with a confocal fluorescence microscope (FV1000 instrument, Olympus).  
50  
51  
52  
53  
54  
55  
56

57  
58 ***In vivo* experiments.** All animal experimental procedures were undertaken  
59  
60

1  
2  
3  
4 following the National Institutes of Health Animal Care and Use Committee protocol.  
5  
6 The Animal Care and Use Committee of Fudan University reviewed the experimental  
7  
8 protocols prior to work beginning and granted ethical approval for all experiments.  
9  
10 Female athymic nude mice aged 4–6 weeks were obtained from Nanjing PengSheng  
11  
12 Biological Technology Co., Ltd and injected with  $1 \times 10^6$  4T1 cells (100  $\mu$ L of cell  
13  
14 suspension). When the tumor volumes (calculated as  $V=W^2 \times L/2$ , where L and W  
15  
16 denote the length width and width of the tumor) extended to 50 mm<sup>3</sup> the animals were  
17  
18 divided randomly into 5 treatment groups (n = 5 each group) as follows: saline,  
19  
20 MoO<sub>x</sub>-PEG-Mel+NIR, free DOX, MoO<sub>x</sub>-PEG-Mel-DOX and  
21  
22 MoO<sub>x</sub>-PEG-Mel-DOX+NIR at 3 mg/kg equivalent concentrations of DOX. In the  
23  
24 MoO<sub>x</sub>-PEG-Mel+NIR group, the same mas of nanosheets as for the  
25  
26 MoO<sub>x</sub>-PEG-Mel-DOX groups was used. 24 h after injection, the mice were  
27  
28 anesthetized and the animals in the NIR groups were exposing with an 808 nm NIR  
29  
30 laser (1 W/cm<sup>2</sup>) for 10 min at the tumor site. Tumor volumes and animal body  
31  
32 weights were recorded every three days after irradiation and the survival curves  
33  
34 evaluated by Kaplan-Meier analysis <sup>57</sup>.  
35  
36  
37  
38  
39  
40  
41  
42  
43  
44

45 **Histological analysis.** After a treatment period of 21 days, the mice were  
46  
47 euthanized using carbon dioxide suffocation and the major organs were harvested.  
48  
49 The majore organs and tumors were fixed in 10% formalin, embedded in paraffin, and  
50  
51 stained with H&E. The sections were then studied using a digital microscope (Leica  
52  
53 Qwin). Terminal deoxynucleotidyl transferase dUTP nick end labeling (TUNEL)  
54  
55 staining was employed to explore the cellular death processes in the tumor in terms of  
56  
57  
58  
59  
60

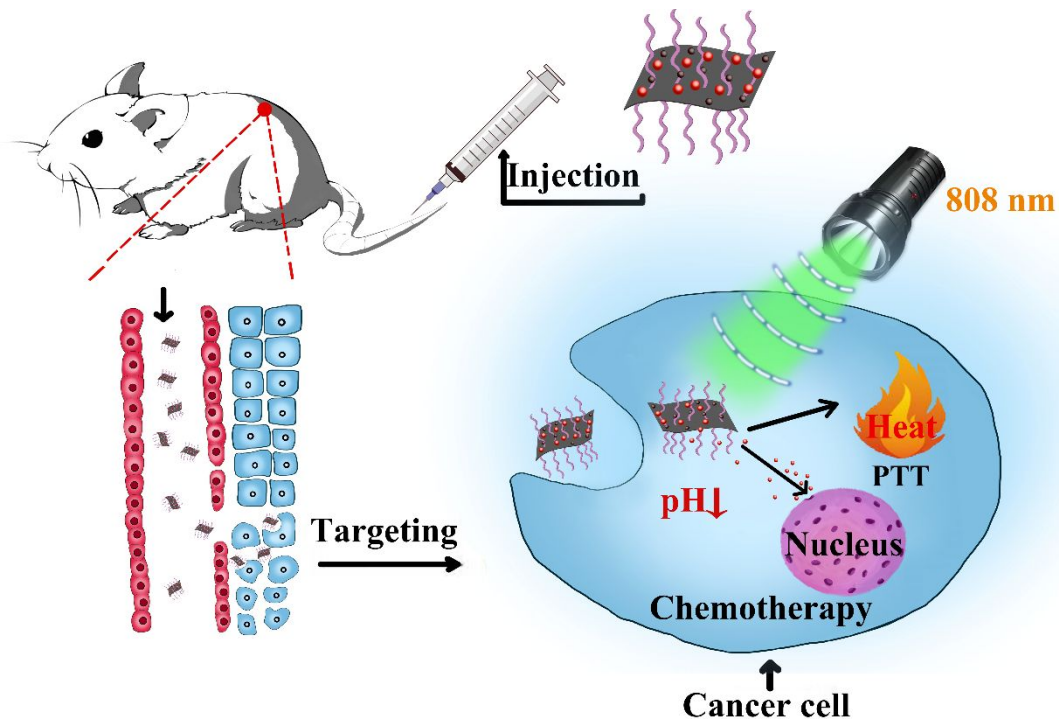
1  
2  
3  
4 the manufacturer's specification.  
5

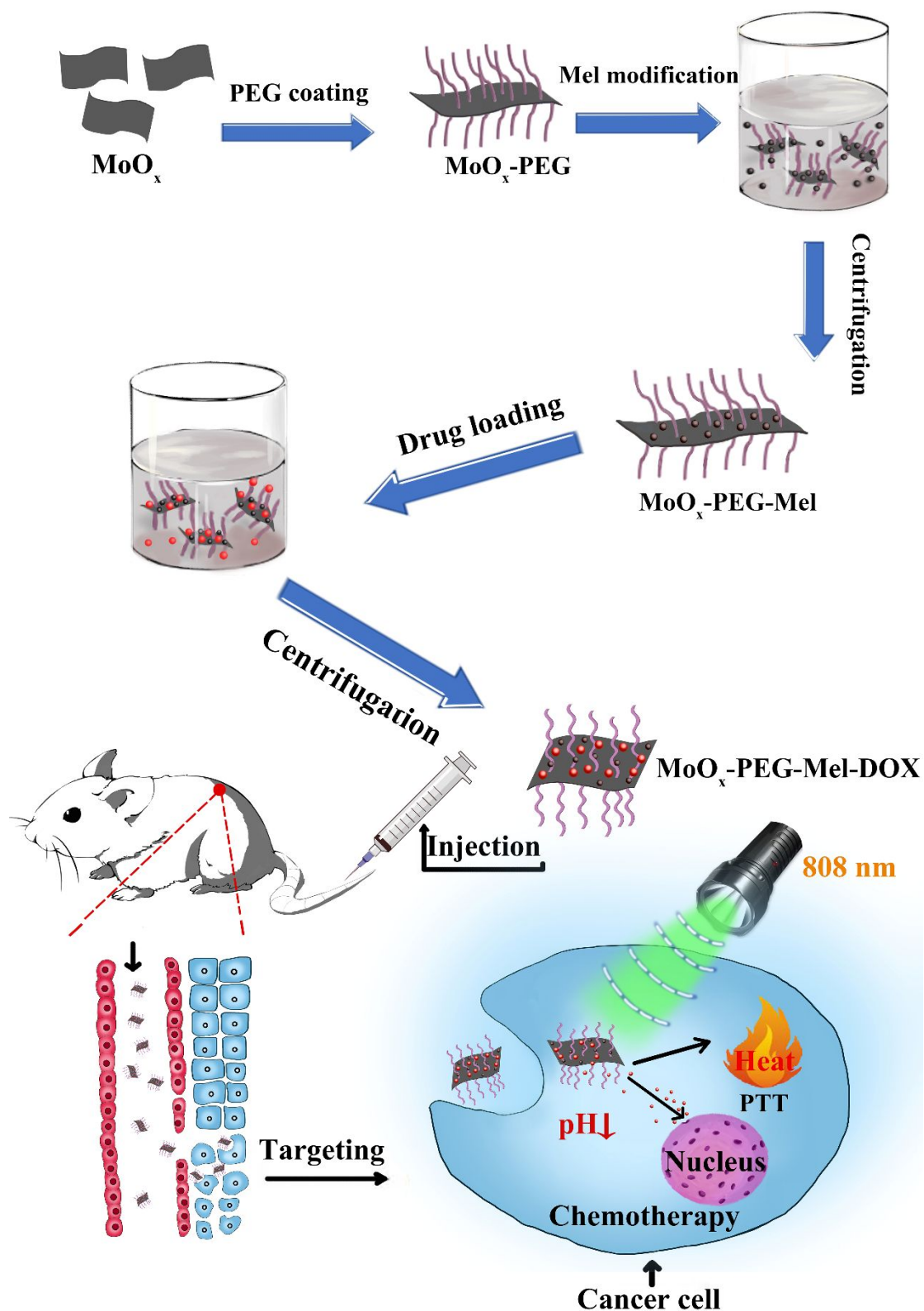
6 **Biodistribution study.** Female athymic nude mice aged 4-6 weeks bearing 4T1  
7  
8 murine breast cancer tumors were euthanized at selected time points after the  
9  
10 intravenous injection of MoOx-PEG-Mel-DOX (200 $\mu$ L, 20mg/kg). Sacrifices (four  
11  
12 mice per time point) took place on one, three and seven days after administration. The  
13  
14 major organs (heart, liver, spleen, lungs, kidneys, stomach, intestine, bone, muscle,  
15  
16 skin) were harvested and then solubilized in aqua regia. The biodistribution of  
17  
18 MoOx-PEG-Mel-DOX was investigated by quantifying the concentration of Mo in  
19  
20 the using inductively coupled plasma atomic emission spectroscopy (ICP-AES,  
21  
22 Hudson, NH03051, USA), and is presented as the percentage of injected dose per  
23  
24 gram of blood (% ID/g).  
25  
26  
27  
28  
29  
30  
31

32 **Statistical analysis.** All experiments were repeated at least three times. Data are  
33  
34 shown as mean  $\pm$  standard deviation (S.D.). The Origin 8.5 software was used to  
35  
36 perform statistical analysis. A Student's t-test was used to compare two independent  
37  
38 groups of data, and statistical significance was considered to be reached at  $P < 0.05$   
39  
40  
41  
42  
43 (\*),  $P < 0.01$  (\*\*) and  $P < 0.001$  (\*\*\*).  
44  
45  
46  
47  
48  
49  
50  
51  
52  
53  
54  
55  
56  
57  
58  
59  
60

1  
2  
3  
4  
5  
6  
7  
8  
9  
10  
11  
12  
13  
14  
15  
16  
17  
18  
19  
20  
21  
22  
23  
24  
25  
26  
27  
28  
29  
30  
31  
32  
33  
34  
35  
36  
37  
38  
39  
40  
41  
42  
43  
44  
45  
46  
47  
48  
49  
50  
51  
52  
53  
54  
55  
56  
57  
58  
59  
60

**Graphic abstract**





**Scheme 1.** Schematic for construction and synergistic therapy of the MoO<sub>x</sub>-PEG-Mel-DOX nanoplatform.

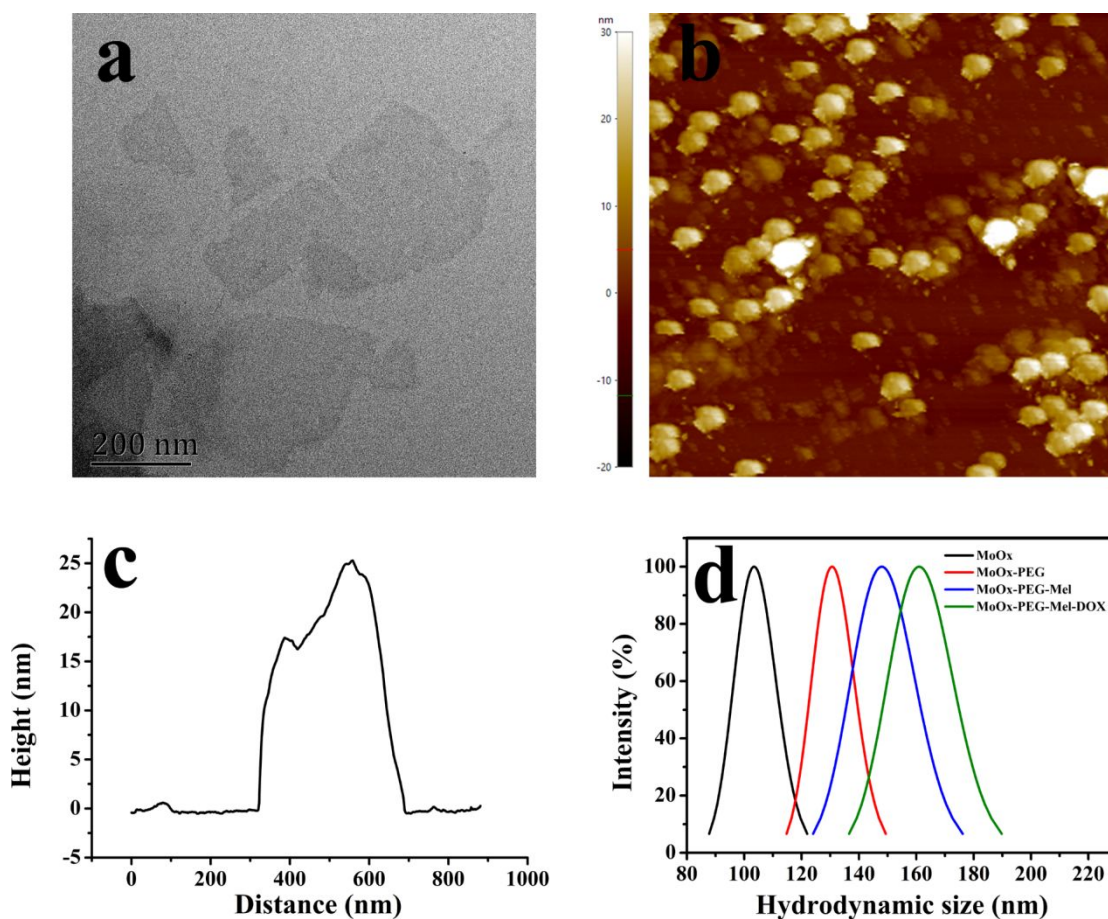


**Figure 1.** (a) TEM image of the MoO<sub>x</sub> nanosheets. (b) AFM image of MoO<sub>x</sub> with (c) the corresponding AFM height profile. (d) DLS data on MoO<sub>x</sub> and its derivatives.

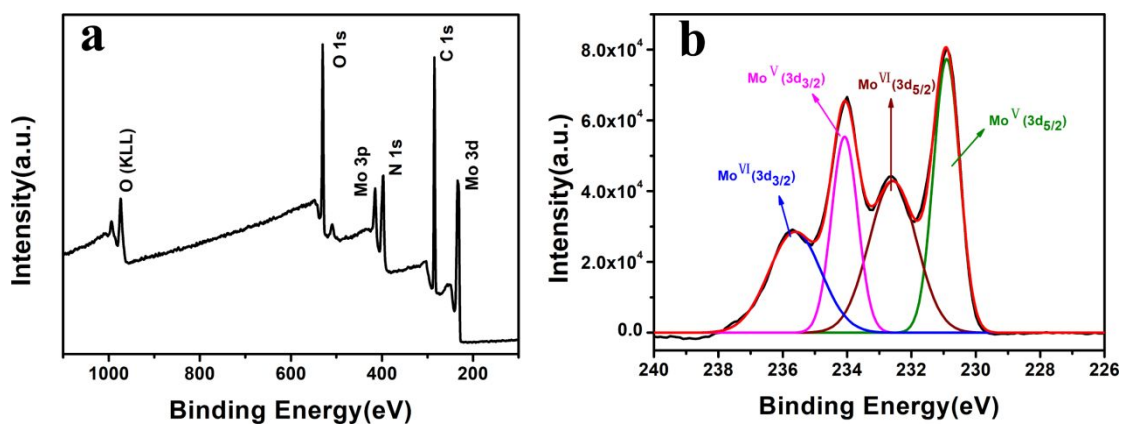


**Figure 2.** XPS data showing (a) a survey spectrum and (b) the Mo 3d region.

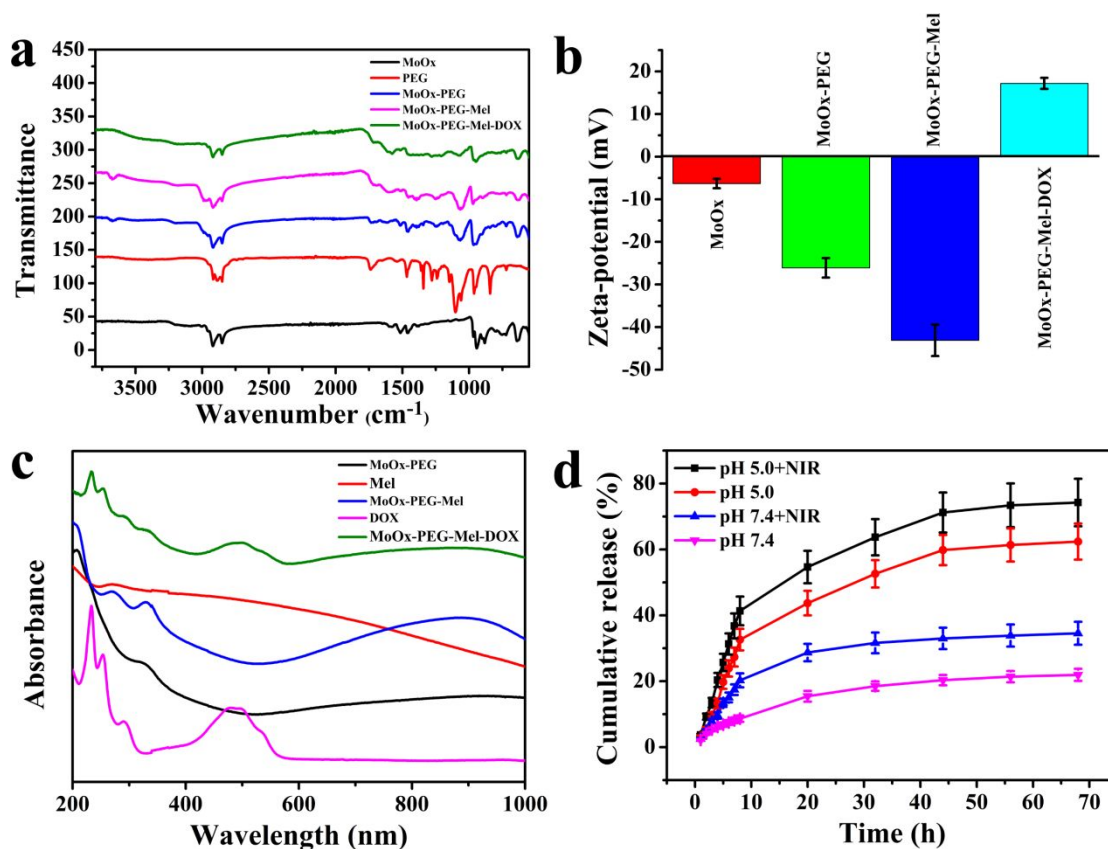


**Figure 3.** Characterizing data verifying the sequential functionalization steps, and drug release profiles. (a) FT-IR spectra. (b) Zeta potential values ( $n = 3$ , mean  $\pm$  S.D.). (c) UV-Vis-NIR spectra. (d) DOX release profiles under different pH values and with or without 808 nm laser irradiation ( $1 \text{ W/cm}^2$  for 5 min at 1, 5, 12, 24, 48, and 60 h) ( $n = 3$ , mean  $\pm$  S.D.)

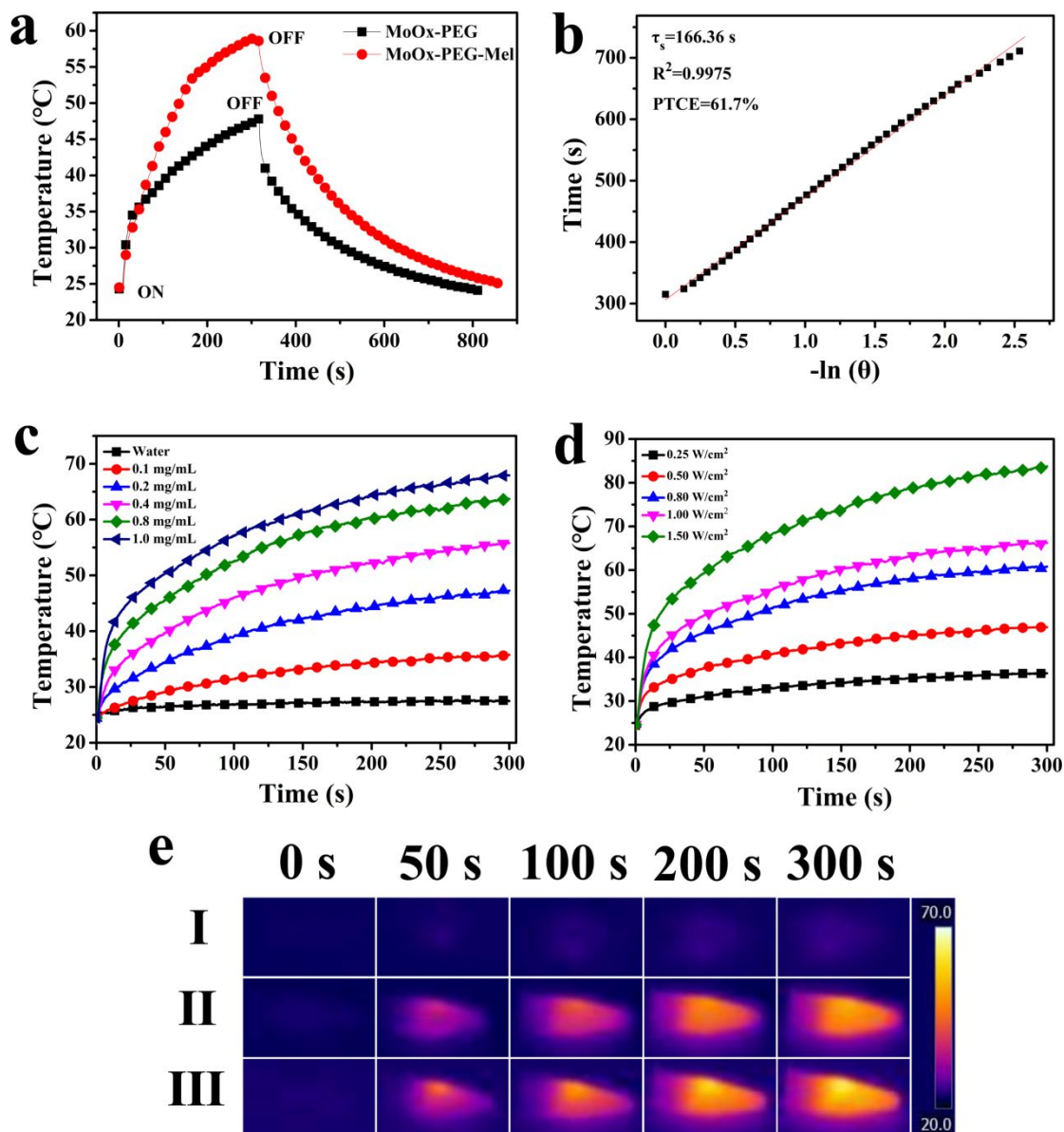


**Figure 4.** (a) The temperature changes induced in suspensions of MoO<sub>x</sub>-PEG and MoO<sub>x</sub>-PEG-Mel under 808 nm NIR irradiation. (b) A plot of time vs  $\ln(\theta)$  for MoO<sub>x</sub>-PEG-Mel, obtained from the cooling period. (c) Temperature vs time curves for suspensions of MoO<sub>x</sub>-PEG-Mel-DOX at different concentrations (laser: 1 W/cm<sup>2</sup>, 5 min). (d) Temperature vs time curves for MoO<sub>x</sub>-PEG-Mel-DOX suspensions (1 mg mL<sup>-1</sup>) exposed to different laser power densities. (e) Photothermal images of (I) water, (II) MoO<sub>x</sub>-PEG and (III) MoO<sub>x</sub>-PEG-Mel (1 mg/mL) under 808 nm laser irradiation (1 W/cm<sup>2</sup>).

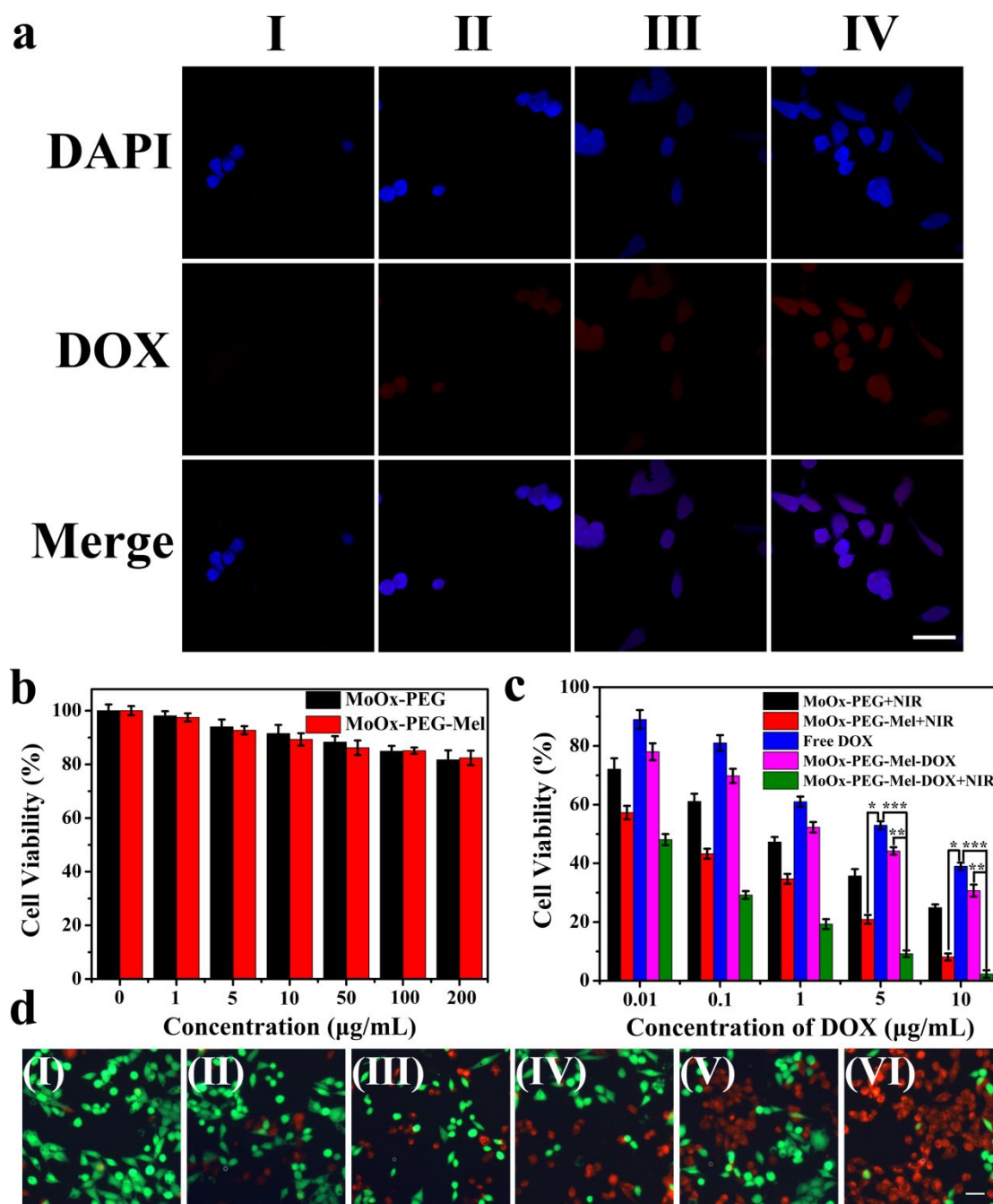


**Figure 5.** (a) Fluorescence images of 4T1 cells incubated with different solutions ( I : PBS, II : free DOX, III : MoO<sub>x</sub>-PEG-Mel-DOX and IV : MoO<sub>x</sub>-PEG-Mel-DOX+NIR). *In vitro* cell culture results showing the viability of 4T1 cells exposed to (b) various concentrations of MoO<sub>x</sub>-PEG and MoO<sub>x</sub>-PEG-Mel; (c) MoO<sub>x</sub>-PEG+NIR, MoO<sub>x</sub>-PEG-Mel+NIR, free DOX, and MoO<sub>x</sub>-PEG-Mel-DOX with

or without NIR. (d) Fluorescence images of 4T1 cells after CA/PI staining: ( I ) PBS+NIR, ( II ) free DOX, ( III ) MoO<sub>x</sub>-PEG-Mel-DOX, ( IV ) MoO<sub>x</sub>-PEG+NIR, ( V ) MoO<sub>x</sub>-PEG-Mel+NIR, and ( VI ) MoO<sub>x</sub>-PEG-Mel-DOX+NIR (all with equivalent concentrations of DOX). Laser power density: 1 W cm<sup>-2</sup>; scale bar: 50 μm test. \*\* denotes P < 0.01, and \*\*\*P < 0.001 (calculated from a Student's T-test). Three separated experiments were conducted and there were five replicates each time.

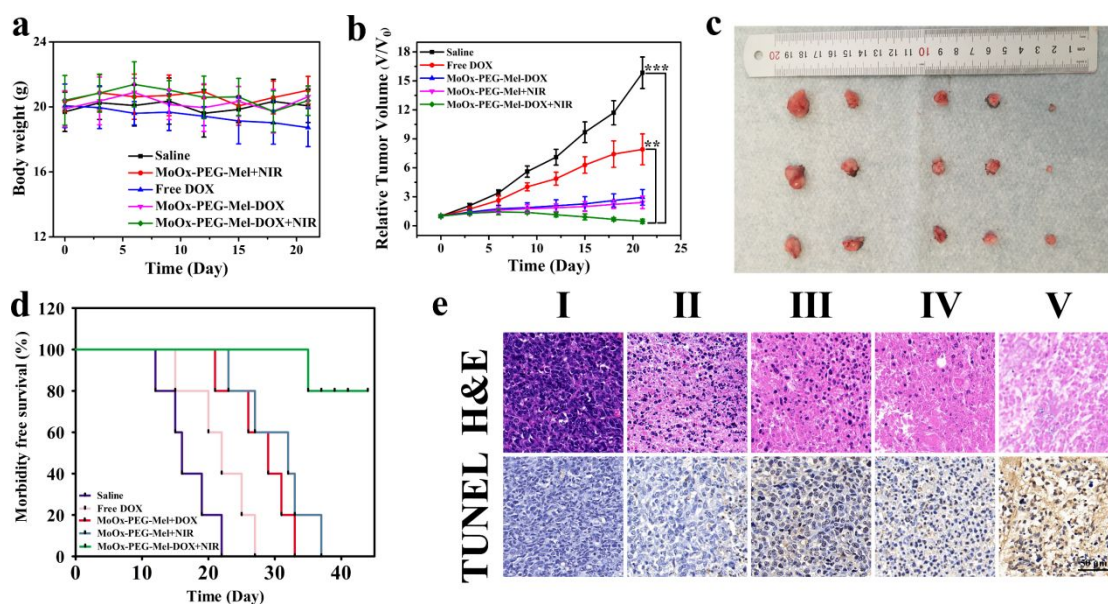
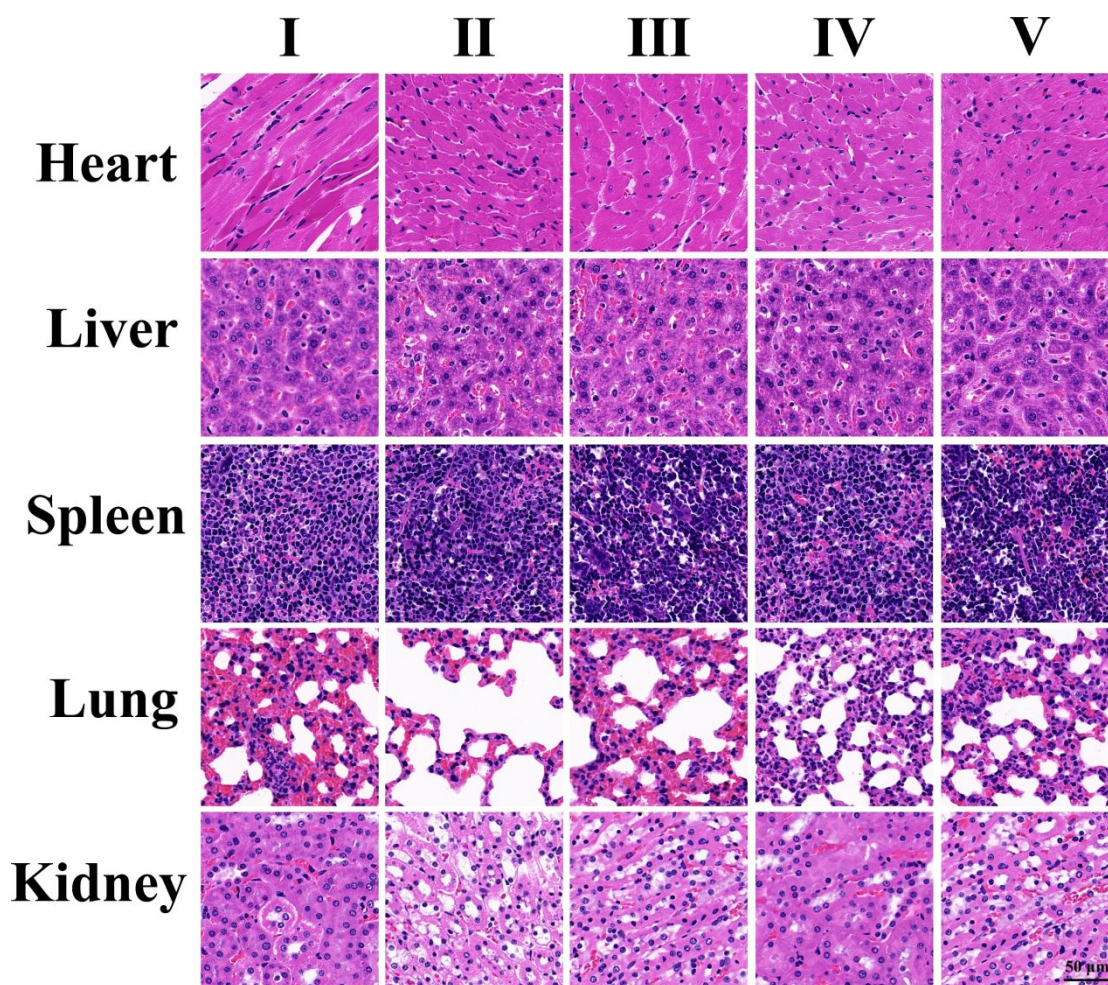


**Figure 6.** The results of *in vivo* antitumor efficacy experiments. (a) Average body weight variation with time. (b) The evolution of tumor volume. \*\*p < 0.01, and \*\*\*p < 0.001 (Student's t test). (c) Representative photographs of tumors exercised on day 21. (d) Kaplan-Meier survival curves. (e) Histological analysis (H&E staining and TUNEL staining) of tumors from mice receiving ( I ) control (saline); ( II ) free DOX; ( III ) MoO<sub>x</sub>-PEG-Mel-DOX; ( IV ) MoO<sub>x</sub>-PEG-Mel+NIR; and, ( V ) MoO<sub>x</sub>-PEG-Mel-DOX+NIR (Scale bars: 50 μm).



35 **Figure 7.** Representative H&E-stained sections from mice receiving the varied  
36 treatments: ( I ) control (saline); ( II ) free DOX; ( III ) MoO<sub>x</sub>-PEG-Mel-DOX; ( IV )  
37 MoO<sub>x</sub>-PEG-Mel+NIR; ( V ) MoO<sub>x</sub>-PEG-Mel-DOX+NIR. Scale bars: 50 μm.  
38  
39  
40  
41  
42  
43  
44  
45  
46  
47  
48  
49  
50  
51  
52  
53  
54  
55  
56  
57  
58  
59  
60

## ASSOCIATED CONTENT

### Supporting Information

XRD patterns of the MoO<sub>x</sub> nanomaterials, a plot to calculate the PTCE of MoO<sub>x</sub>-PEG, data showing the photothermal stability of MoO<sub>x</sub>-PEG-Mel-DOX and optimization of drug loading, the results of a study into cellular uptake by flow cytometry, and the findings from *in vivo* biodistribution studies in mice.

## AUTHOR INFORMATION

### Corresponding Authors

\*E-mail: lzhu@dhu.edu.cn.

\*E-mail: 377453507@qq.com.

### ORCID

Li-min Zhu: 0000-0003-2806-7971

### Conflict of Interest

The authors declare no conflict of interest.

## ACKNOWLEDGEMENTS

This research was financially supported by the Shanghai Municipal Science and Technology Commission Project (grant 16410723700), the Outstanding Clinical Discipline Project of Shanghai Pudong (Grant No. PWYgy2018-09), the UK-China Joint Laboratory for Therapeutic Textiles (based at Donghua University), and the

1  
2  
3  
4 Biomedical Textile Materials "111 Project" of the China Ministry of Education (No  
5  
6 B07024).  
7  
8  
9  
10  
11  
12  
13  
14  
15  
16  
17  
18  
19  
20  
21  
22  
23

## 24 REFERENCES

- 25  
26  
27 (1) Ferrari, M. Cancer nanotechnology: opportunities and challenges. *Nat. Rev.*  
28 *Cancer* **2005**, *5*, 161-171.  
29  
30  
31  
32 (2) Laura Martínez, M.; Patricia, H. G.; Blanca, D. R.; Julio, R.; Caamano, A. J.;  
33  
34 Elisa, C.; Angeles, J.; Francisco, S. R.; José García, S.; Daniel, J. Heating efficiency  
35  
36 of multi-walled carbon nanotubes in the first and second biological windows.  
37  
38 *Nanoscale* **2013**, *5*, 7882-7889.  
39  
40  
41  
42 (3) Lev, D.; Nikolai, K. Gold nanoparticles in biomedical applications: recent  
43  
44 advances and perspectives. *Chem. Soc. Rev.* **2012**, *41*, 2256-2282.  
45  
46  
47 (4) Li, J.; Hu, Y.; Yang, J.; Wei, P.; Sun, W.; Shen, M.; Zhang, G.; Shi, X. Hyaluronic  
48  
49 acid-modified Fe<sub>3</sub>O<sub>4</sub>@Au core/shell nanostars for multimodal imaging and  
50  
51 photothermal therapy of tumors. *Biomaterials* **2015**, *38*, 10-21.  
52  
53  
54 (5) Li, X.; Xing, L.; Zheng, K.; Wei, P.; Du, L.; Shen, M.; Shi, X. Formation of Gold  
55  
56 Nanostar-Coated Hollow Mesoporous Silica for Tumor Multimodality Imaging and  
57  
58  
59  
60

- 1  
2  
3  
4 Photothermal Therapy. *ACS Appl. Mater. Interfaces* **2017**, *9*, 5817-5827.  
5  
6 (6) Vijayakumar, S.; Selvakumar, S.; Chen-Sheng, Y. Near-infrared light-responsive  
7  
8 nanomaterials in cancer therapeutics. *Chem. Soc. Rev.* **2014**, *43*, 6254-6287.  
9  
10  
11 (7) Xia, B.; Wang, B.; Shi, J.; Zhang, Y.; Zhang, Q.; Chen, Z.; Li, J. Photothermal and  
12  
13 biodegradable polyaniline/porous silicon hybrid nanocomposites as drug carriers for  
14  
15 combined chemo-photothermal therapy of cancer. *Acta Biomater.* **2017**, *51*, 197-208.  
16  
17  
18 (8) Xianguang, D.; Hao, L. C.; Mengxin, Z.; Renjun, H.; Chunyan, L.; He, S.;  
19  
20 Mengya, L.; Yu, Z.; Nan, G.; Zhijun, Z. Surface plasmon resonance enhanced light  
21  
22 absorption and photothermal therapy in the second near-infrared window. *J. Am.*  
23  
24  
25  
26  
27  
28  
29  
30 (9) Wu, J.; Williams, G. R.; Niu, S.; Gao, F.; Tang, R.; Zhu, L. M. A Multifunctional  
31  
32 Biodegradable Nanocomposite for Cancer Theranostics. *Adv. Sci.* **2019**, *10*, 1802001.  
33  
34  
35 (10) Kai, Y.; Liangzhu, F.; Xiaoze, S.; Zhuang, L. Nano-graphene in biomedicine:  
36  
37  
38  
39  
40  
41  
42  
43  
44  
45  
46  
47  
48  
49  
50  
51  
52  
53  
54  
55  
56  
57  
58  
59  
60  
60 (11) Liu, J.; Yu, M.; Zhou, C.; Yang, S.; Ning, X.; Zheng, J. Passive tumor targeting  
of renal-clearable luminescent gold nanoparticles: long tumor retention and fast  
normal tissue clearance. *J. Am. Chem. Soc.* **2013**, *135*, 4978-4981.  
  
(12) Chen, J.; Li, X.; Liu, X.; Yan, H.; Xie, Z.; Sheng, Z.; Gong, X.; Wang, L.; Liu,  
X.; Zhang, P. Hybrid MoSe<sub>2</sub>-Indocyanine Green Nanosheets as A High-Efficient  
Phototheranostic Agent for Photoacoustic Imaging Guided Photothermal Cancer  
Therapy. *Biomater. Sci.* **2018**, *6*, 1503-1516.  
  
(13) Wang, K.; Zhang, Y.; Wang, J.; Yuan, A.; Sun, M.; Wu, J.; Hu, Y.

1  
2  
3  
4 Self-assembled IR780-loaded transferrin nanoparticles as an imaging, targeting and  
5  
6 PDT/PTT agent for cancer therapy. *Sci Rep* **2016**, *6*, 27421.  
7

8  
9 (14) Lin, H.; Feng, Q.; Wang, Y.; Zhang, H.; Jiang, G.; Yang, X.; Ren, J.; Zhu, X.;  
10  
11 Shi, Y.; Zhang, Z. Multifunctional nanosheets based on hyaluronic acid modified  
12  
13 graphene oxide for tumor-targeting chemo-photothermal therapy. *J. Nanopart. Res.*  
14  
15 **2015**, *17*, 162.  
16  
17

18  
19 (15) Teng, L.; Chao, W.; Xing, G.; Hua, G.; Liang, C.; Xiaoze, S.; Liangzhu, F.;  
20  
21 Baoquan, S.; Zhuang, L. Drug delivery with PEGylated MoS<sub>2</sub> nano-sheets for  
22  
23 combined photothermal and chemotherapy of cancer. *Adv. Mater.* **2014**, *26*,  
24  
25 3433-3440.  
26  
27

28  
29 (16) Zhang, X.; Wu, J.; Williams, G. R.; Yang, Y.; Niu, S.; Qian, Q.; Zhu, L. M.  
30  
31 Dual-responsive molybdenum disulfide/copper sulfide-based delivery systems for  
32  
33 enhanced chemo-photothermal therapy. *J. Colloid Interface Sci.* **2019**, *539*, 433-441.  
34  
35

36  
37 (17) Han, X.; Huang, J.; Lin, H.; Wang, Z.; Li, P.; Chen, Y. 2D Ultrathin  
38  
39 MXene-Based Drug-Delivery Nanoplatfrom for Synergistic Photothermal Ablation  
40  
41 and Chemotherapy of Cancer. *Adv. Healthc. Mater.* **2018**, *7*, 1701394.  
42  
43

44  
45 (18) Tianyue, J.; Wujin, S.; Qiuwen, Z.; Burns, N. A.; Khan, S. A.; Ran, M.; Zhen, G.  
46  
47 Furin-mediated sequential delivery of anticancer cytokine and small-molecule drug  
48  
49 shuttled by graphene. *Adv. Mater.* **2015**, *27*, 1021-1028.  
50  
51

52  
53 (19) Liang, C.; Chao, Y.; Sida, S.; Xuan, Y.; Hua, G.; Kai, Y.; Zhuang, L. Bottom-Up  
54  
55 Synthesis of Metal-Ion-Doped WS<sub>2</sub> Nanoflakes for Cancer Theranostics. *ACS Nano*  
56  
57 **2015**, *9*, 11090-11101.  
58  
59  
60

- 1  
2  
3  
4 (20) Kim, H. Near-infrared light-responsive nanomaterials for cancer theranostics.  
5  
6 *Wiley Interdiscip. Rev.-Nanomed. Nanobiotechnol.* **2016**, *8*, 23-45.  
7  
8  
9 (21) Bao, T.; Yin, W.; Zheng, X.; Zhang, X.; Yu, J.; Dong, X.; Yong, Y.; Gao, F.;  
10  
11 Yan, L.; Gu, Z.; Zhao, Y. One-pot synthesis of PEGylated plasmonic MoO<sub>(3-x)</sub> hollow  
12  
13 nanospheres for photoacoustic imaging guided chemo-photothermal combinational  
14  
15 therapy of cancer. *Biomaterials* **2016**, *76*, 11-24.  
16  
17  
18 (22) Kai, D.; Zhen, L.; Zhenhua, L.; Jinsong, R.; Xiaogang, Q. Hydrophobic  
19  
20 anticancer drug delivery by a 980 nm laser-driven photothermal vehicle for efficient  
21  
22 synergistic therapy of cancer cells in vivo. *Adv. Mater.* **2013**, *25*, 4452-4458.  
23  
24  
25 (23) Fauchaux, J. A.; Stanton, A. L.; Jain, P. K. Plasmon Resonances of  
26  
27 Semiconductor Nanocrystals: Physical Principles and New Opportunities. *J. Phys.*  
28  
29 *Chem. Lett.* **2014**, *5*, 976-985.  
30  
31  
32 (24) Marin, B. C.; Hsu, S. W.; Li, C.; Lo, A.; Zwissler, D. W.; Liu, Z.; Tao, A. R.  
33  
34 Plasmon-Enhanced Two-Photon Absorption in Photoluminescent Semiconductor  
35  
36 Nanocrystals. *ACS Photonics* **2016**, *3*, 526-531.  
37  
38  
39 (25) Murray, W. A.; Barnes, W. L. Plasmonic materials. *Adv. Mater.* **2007**, *19*,  
40  
41 3771-3782.  
42  
43  
44 (26) Liu, W.; Li, X.; Li, W.; Zhang, Q.; Bai, H.; Li, J.; Xi, G. Highly stable  
45  
46 molybdenum dioxide nanoparticles with strong plasmon resonance are promising in  
47  
48 photothermal cancer therapy. *Biomaterials* **2018**, *163*, 43-54.  
49  
50  
51 (27) Yin, W.; Bao, T.; Zhang, X.; Gao, Q.; Yu, J.; Dong, X.; Yan, L.; Gu, Z.; Zhao,  
52  
53  
54  
55  
56  
57  
58  
59  
60 Y. Biodegradable MoO<sub>x</sub> nanoparticles with efficient near-infrared photothermal and

1  
2  
3  
4 photodynamic synergetic cancer therapy at the second biological window. *Nanoscale*  
5  
6 **2018**, *10*, 1517-1531.

7  
8  
9 (28) Riley, P. A. Melanin. *Int. J. Biochem. Cell Biol.* **1997**, *29*, 1235-1239.

10  
11 (29) Yanlan, L.; Kelong, A.; Jianhua, L.; Mo, D.; Yangyang, H.; Lehui, L.  
12  
13 Dopamine-melanin colloidal nanospheres: an efficient near-infrared photothermal  
14  
15 therapeutic agent for in vivo cancer therapy. *Adv. Mater.* **2013**, *25*, 1353-1359.

16  
17 (30) Jiang, Q.; Luo, Z.; Men, Y.; Yang, P.; Peng, H.; Guo, R.; Tian, Y.; Pang, Z.;  
18  
19 Yang, W. Red blood cell membrane-camouflaged melanin nanoparticles for enhanced  
20  
21 photothermal therapy. *Biomaterials* **2017**, *143*, 29-45.

22  
23 (31) Cho, S.; Park, W.; Kim, D. H. Silica-Coated Metal Chelating-Melanin  
24  
25 Nanoparticles as a Dual-Modal Contrast Enhancement Imaging and Therapeutic  
26  
27 Agent. *ACS Appl. Mater. Interfaces* **2017**, *9*, 101-111.

28  
29 (32) Xiaoxin, Q.; Sida, S.; Teng, L.; Liang, C.; Zhuang, L. Two-dimensional TiS<sub>2</sub>  
30  
31 nanosheets for in vivo photoacoustic imaging and photothermal cancer therapy.  
32  
33 *Nanoscale* **2015**, *7*, 6380-6387.

34  
35 (33) Song, G.; Hao, J.; Liang, C.; Liu, T.; Gao, M.; Cheng, L.; Hu, J.; Liu, Z.  
36  
37 Degradable Molybdenum Oxide Nanosheets with Rapid Clearance and Efficient  
38  
39 Tumor Homing Capabilities as a Therapeutic Nanoplatfom. *Angew. Chem.-Int. Edit.*  
40  
41 **2016**, *55*, 2122-2126.

42  
43 (34) Ainwar, M.; Hogarth, C. A.; Theocharis, C. R. A study of the infrared absorption  
44  
45 spectra of thin amorphous films of molybdenum trioxide. *J. Mater. Sci.* **1989**, *24*,  
46  
47 2387-2390.

1  
2  
3  
4 (35) Bhosle, V.; Tiwari, A.; Narayan, J. Epitaxial growth and properties of  
5  
6 MoO<sub>x</sub>(2<x<2.75) films. *J. Appl. Phys.* **2005**, *97*, 083539.

7  
8  
9 (36) Katrib, A.; Petit, C.; Légaré, P.; Hilaire, L.; Maire, G. An investigation of  
10  
11 metal-support interaction in bimetallic Pt-Mo catalysts deposited on silica and  
12  
13 alumina. *Surf. Sci.* **1987**, *189*, 886-893.

14  
15  
16 (37) Kumar, V.; Wang, X.; Lee, P. S. Synthesis of pyramidal and prismatic hexagonal  
17  
18 MoO<sub>3</sub> nanorods using thiourea. *Crystengcomm* **2013**, *15*, 7663-7669.

19  
20 (38) Pandey, S.; Sharma, K. H.; Sharma, A. K.; Nerthigan, Y.; Hang, D. R.; Wu, H. F.  
21  
22 Comparative Photothermal Performance among Various Sub-Stoichiometric 2D  
23  
24 Oxygen-Deficient Molybdenum Oxide Nanoflakes and In Vivo Toxicity. *Chem.-Eur.*  
25  
26 *J.* **2018**, *24*, 7417-7427.

27  
28 (39) Song, G.; Shen, J.; Jiang, F.; Hu, R.; Li, W.; An, L.; Zou, R.; Chen, Z.; Qin, Z.;  
29  
30 Hu, J. Hydrophilic molybdenum oxide nanomaterials with controlled morphology and  
31  
32 strong plasmonic absorption for photothermal ablation of cancer cells. *ACS Appl.*  
33  
34 *Mater. Interfaces* **2014**, *6*, 3915-3922.

35  
36 (40) Wongkrua, P.; Thongtem, T.; Thongtem, S. Synthesis of h- and α-MoO<sub>3</sub> by  
37  
38 Refluxing and Calcination Combination: Phase and Morphology Transformation,  
39  
40 Photocatalysis, and Photosensitization. *J. Nanomater.* **2013**, *8*, 702679.

41  
42 (41) Zhan, Y.; Liu, Y.; Zu, H.; Guo, Y.; Wu, S.; Yang, H.; Liu, Z.; Lei, B.; Zhuang,  
43  
44 J.; Zhang, X.; Huang, D.; Hu, C. Phase-controlled synthesis of molybdenum oxide  
45  
46 nanoparticles for surface enhanced Raman scattering and photothermal therapy.  
47  
48 *Nanoscale* **2018**, *10*, 5997-6004.

1  
2  
3  
4 (42) Zhang, X.; Wu, J.; Williams, G. R.; Niu, S.; Qian, Q.; Zhu, L. M. Functionalized  
5  
6 MoS<sub>2</sub>-nanosheets for targeted drug delivery and chemo-photothermal therapy. *Colloid*  
7  
8 *Surf. B-Biointerfaces* **2019**, *173*, 101-108.

9  
10  
11 (43) Jin, J.; Guo, M.; Liu, J.; Liu, J.; Zhou, H.; Li, J.; Wang, L.; Liu, H.; Li, Y.; Zhao,  
12  
13 Y.; Chen, C. Graphdiyne Nanosheet-Based Drug Delivery Platform for  
14  
15 Photothermal/Chemotherapy Combination Treatment of Cancer. *ACS Appl. Mater.*  
16  
17 *Interfaces* **2018**, *10*, 8436-8442.

18  
19  
20 (44) Xu, Y.; Hu, X.; Guan, P.; Du, C.; Tian, Y.; Ding, S.; Li, Z.; Yan, C. A novel  
21  
22 controllable molecularly imprinted drug delivery system based on the photothermal  
23  
24 effect of graphene oxide quantum dots. *J. Mater. Sci.* **2019**, *54*, 9124-9139.

25  
26  
27 (45) Wu, P.; Wang, X.; Wang, Z.; Ma, W.; Guo, J.; Chen, J.; Yu, Z.; Li, J.; Zhou, D.  
28  
29 Light-Activatable Prodrug and AIEgen Copolymer Nanoparticle for Dual-Drug  
30  
31 Monitoring and Combination Therapy. *ACS Appl. Mater. Interfaces* **2019**, *11*,  
32  
33 18691-18700.

34  
35  
36 (46) Cheng, Y.-J.; Qin, S.-Y.; Ma, Y.-H.; Chen, X.-S.; Zhang, A.-Q.; Zhang, X.-Z.  
37  
38 Super-pH-Sensitive Mesoporous Silica Nanoparticle-Based Drug Delivery System for  
39  
40 Effective Combination Cancer Therapy. *ACS Biomater. Sci. Eng.* **2019**, *5*, 1878-1886.

41  
42  
43 (47) Liu, T.; Wang, C.; Gu, X.; Gong, H.; Cheng, L.; Shi, X.; Feng, L.; Sun, B.; Liu,  
44  
45 Z. Drug delivery with PEGylated MoS<sub>2</sub> nano-sheets for combined photothermal and  
46  
47 chemotherapy of cancer. *Adv. Mater.* **2014**, *26*, 3433-3440.

48  
49  
50 (48) Niu, S.; Bremner, D. H.; Wu, J.; Wu, J.; Wang, H.; Li, H.; Qian, Q.; Zheng, H.;  
51  
52 Zhu, L. l-Peptide functionalized dual-responsive nanoparticles for controlled  
53  
54  
55  
56  
57  
58  
59  
60

1  
2  
3  
4 paclitaxel release and enhanced apoptosis in breast cancer cells. *Drug Deliv.* **2018**, *25*,  
5  
6 1275-1288.

7  
8  
9 (49) Chen, Y. W.; Su, Y. L.; Hu, S. H.; Chen, S. Y. Functionalized graphene  
10  
11 nanocomposites for enhancing photothermal therapy in tumor treatment. *Adv. Drug*  
12  
13 *Deliv. Rev.* **2016**, *105*, 190-204.

14  
15  
16 (50) Tao, W.; Ji, X.; Xu, X.; Islam, M. A.; Li, Z.; Chen, S.; Saw, P. E.; Zhang, H.;  
17  
18 Bharwani, Z.; Guo, Z.; Shi, J.; Farokhzad, O. C. Antimonene Quantum Dots:  
19  
20 Synthesis and Application as Near-Infrared Photothermal Agents for Effective Cancer  
21  
22 Therapy. *Angew. Chem.-Int. Edit.* **2017**, *56*, 11896-11900.

23  
24  
25 (51) Xie, Z.; Wang, D.; Fan, T.; Xing, C.; Li, Z.; Tao, W.; Liu, L.; Bao, S.; Fan, D.;  
26  
27 Zhang, H. Black phosphorus analogue tin sulfide nanosheets: synthesis and  
28  
29 application as near-infrared photothermal agents and drug delivery platforms for  
30  
31 cancer therapy. *J. Mat. Chem. B* **2018**, *6*, 4747-4755.

32  
33  
34 (52) Chen, Y.; Z, F.; Z, Z.; W, N.; C, L.; N, Y.; B, C.; H, Z. Two-Dimensional Metal  
35  
36 Nanomaterials: Synthesis, Properties, and Applications. *Chem. Rev.* **2018**, *118*,  
37  
38 6409-6455.

39  
40  
41 (53) Fan, W.; Yung, B.; Huang, P.; Chen, X. Nanotechnology for Multimodal  
42  
43 Synergistic Cancer Therapy. *Chem. Rev.* **2017**, *117*, 13566-13638.

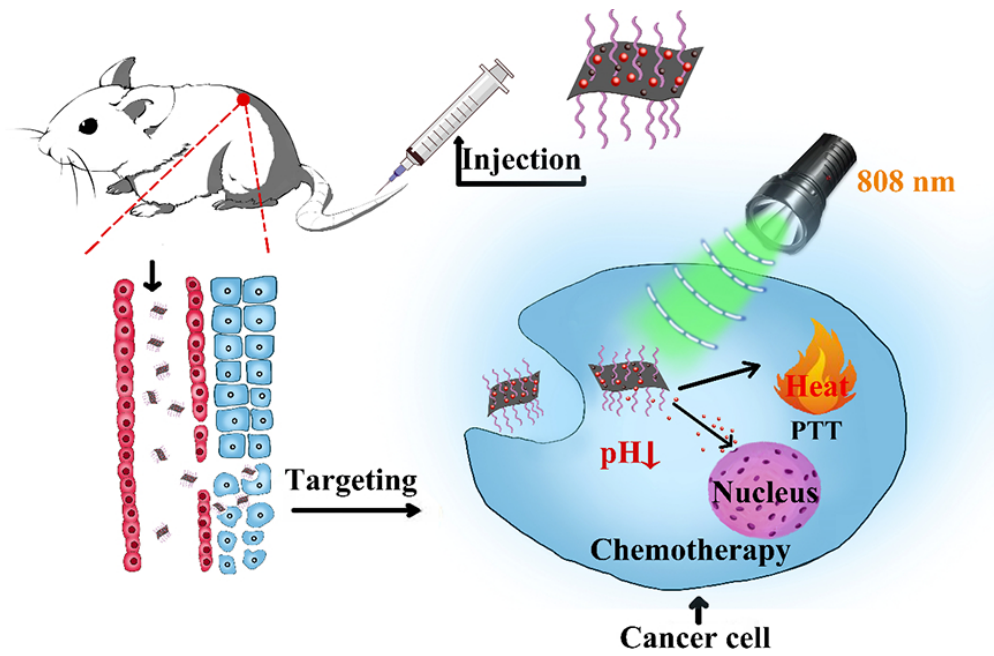
44  
45  
46 (54) Niu, S.; Williams, G. R.; Wu, J.; Wu, J.; Zhang, X.; Zheng, H.; Li, S.; Zhu, L.-M.  
47  
48 A novel chitosan-based nanomedicine for multi-drug resistant breast cancer therapy.  
49  
50  
51  
52  
53  
54  
55  
56 *Chem. Eng. J.* **2019**, *369*, 134-149.

57  
58 (55) Ding, D.; Guo, W.; Guo, C.; Sun, J.; Zheng, N.; Wang, F.; Yan, M.; Liu, S.  
59  
60

1  
2  
3  
4 MoO<sub>3-x</sub> quantum dots for photoacoustic imaging guided photothermal/photodynamic  
5  
6 cancer treatment. *Nanoscale* **2017**, *9*, 2020-2029.

7  
8  
9 (56) Lu, N.; Huang, P.; Fan, W.; Wang, Z.; Liu, Y.; Wang, S.; Zhang, G.; Hu, J.; Liu,  
10  
11 W.; Niu, G. Tri-stimuli-responsive biodegradable theranostics for mild hyperthermia  
12  
13 enhanced chemotherapy. *Biomaterials* **2017**, *126*, 39-48.

14  
15  
16 (57) Martinez-Garcia, M.; Vargas-Barron, J.; Banuelos-Tellez, F.; Gonzalez-Pacheco,  
17  
18 H.; Fresno, C.; Hernandez-Lemus, E.; Martinez-Rios, M. A.; Vallejo, M. Public  
19  
20 insurance program impact on catastrophic health expenditure on acute myocardial  
21  
22 infarction. *Public Health* **2018**, *158*, 47-54.  
23  
24  
25  
26  
27  
28  
29  
30  
31  
32  
33  
34  
35  
36  
37  
38  
39  
40  
41  
42  
43  
44  
45  
46  
47  
48  
49  
50  
51  
52  
53  
54  
55  
56  
57  
58  
59  
60



100x64mm (219 x 219 DPI)